



Lithium-film ceramics for solid-state lithionic devices

Yuntong Zhu¹, Juan Carlos Gonzalez-Rosillo¹, Moran Balaish¹, Zachary D. Hood¹, Kun Joong Kim¹ and Jennifer L. M. Rupp^{1,2}✉

Abstract | The search for alternatives to traditional Li-ion batteries has sparked interest in the chemistry and manufacturing of solid-state Li-ion conductors. Li-ion conductors are traditionally processed as millimetre-sized pellets using conventional ceramic-processing routes. However, in thin-film form, Li-ion conductors offer applications beyond energy storage, including artificial intelligence, in-memory computing and smart sensing. In this Review, we examine the chemistry and thin-film processing of Li oxides and discuss challenges and opportunities for the integration of Li-oxide films in microbatteries for energy storage, neuromorphic computation mimicking human-brain operations and sensors for toxins and greenhouse gases. Li oxides in thin-film form provide fast Li-ion movement and connected electronic-state changes, which improve energy and information density and increase cycle speed and endurance of Li-conductor-based devices. Finally, we provide a future vision of lithionic devices integrating Li-based ceramics for the design of microdevices beyond batteries.

In the course of history, industry has been defined by technical evolution with continual reinvention, depending on the available resources, needs and discoveries. Some industrial advances have had such an overwhelming impact that the associated time periods and achievements have been named ‘industrial revolutions’. For example, mechanization emerged at the end of the eighteenth century, when agriculture was partially replaced by industry, providing a new foundation for the economic structure of society in what is known as the first industrial revolution. The extraction of coal resources and the invention of the steam engine introduced new types of energy conversion. Almost a century later, at the end of the nineteenth century, new sources of energy (that is, oil, gas and electricity) gained in significance, and economic and industrial models based on ‘large factories’ emerged in the second industrial revolution. During this time, the chemical and material manufacturing industry produced goods such as fertilizers, steel and the first functional ceramics. The development of the transistor, which marks the beginning of the third industrial revolution, initiated the birth of electronic-based and information-based technologies that drove the automation of production and computation, as well as the establishment of industries dedicated to the conversion of renewable energy sources and storage technologies, such as batteries. The subsequent exponential increase in computing power and the generation of vast amounts of data, in areas ranging from customer service and policymaking to drug discovery

and materials design, have culminated in the emergence of artificial intelligence (AI) and the beginning of the fourth industrial revolution. The fourth industrial revolution is characterized by the fusion of technologies that cross the boundaries of the digital, physical, material and biological spheres¹, entering cyber-physical production systems and intertwining the real and virtual worlds (Supplementary Fig. 1a).

The evolution of mobile electronic devices, such as phones, computers and medical monitoring units, depends on the performance of their computational units, including light, pressure, chemical and gas sensors, as well as of their energy-storage battery packs. However, these computational units mainly rely on the silicon-based transistor technology from the 1970s². Following Moore’s law, transistors with 5-nm feature size have been produced and commercialized by Samsung Electronics³ and Taiwan Semiconductor Manufacturing Company⁴, with an exponential increase of on-chip transistor density. Nevertheless, quantum-tunnelling effects limit further downscaling of the gate length of transistors and, thus, of transistor-chip densities. Additionally, downscaling and quality verification of chip design are associated with high costs⁵ (Supplementary Fig. 1b). Moreover, computers primarily operate on von Neumann architectures with the data stored in memory and transported to the calculation engine⁶, which requires more energy and computation cycles than the actual computation⁶. The bottleneck of von Neumann architectures limits the computation

¹Department of Materials Science and Engineering, Massachusetts Institute of Technology, Cambridge, MA, USA.

²Department of Electrical Engineering and Computer Science, Massachusetts Institute of Technology, Cambridge, MA, USA.

✉e-mail: jrupp@mit.edu

<https://doi.org/10.1038/s41578-020-00261-0>

speed and throughput of transistor-based logic and results in high energy costs per computing operation⁷. By contrast, AI-based neuromorphic computing and machine-learning algorithms are based on computing architectures that encode and process data based on temporal information of spike events mimicking biological neurons. A clear definition of materials and hardware for artificial neurons in AI and machine-learning operations will greatly contribute to the efforts defined in the fourth industrial revolution (that is, devices that fulfil the needs of the Internet of Things, for example, devices with fast computing and response speed, small size, AI-based algorithms and good biocompatibility) and to the reduction of energy consumption by orders of magnitude compared with von Neumann computing.

Improving the energy density and cycling life of AI-chip-integrated mobile devices will depend on innovations in battery architectures and material components. Current battery packs and sensors are bulky and have functional electrochemical cell entities of $>50\ \mu\text{m}$; for example, liquid-electrolyte-based Li-ion pouch-cell batteries, which are commonly used in mobile phones and other portable electronics. However, electronic devices become more multifunctional and the demand for smaller device sizes and weight, as well as for operation in biocompatible environments, constantly increases. These demands pose challenges for the integration of liquid-electrolyte-based device designs, such as battery pouch cells. Solid-state microbatteries and gas sensors could address these challenges and enable further miniaturization of on-chip devices. The thin-film microbattery market size is predicted to grow by $>40\%$ in 2020 (exceeding US\$1.3 billion by 2021)⁸, which will benefit the development of mobile phones, smart cards and medical implants⁸ (Supplementary Fig. 1c). Similarly, the gas-sensor market size is predicted to grow at a rate of $\sim 6.25\%$ per year and exceed US\$1 billion in 2022 (REF.⁹) (Supplementary Fig. 1d). Gas sensors are predicted to play a key role in medical care, disaster prediction, energy resources and waste management, as well as for the detection of pollutants that affect the environment and in agricultural food production⁹. In particular, the mobile-phone, smart-card and wearables sectors are expected to see the largest growth in the gas-sensor market share. These opportunities and challenges require new materials, manufacturing routes and devices, as well as a thorough understanding of the operational chemistry and physics in gas sensing and autonomous energy supply.

In this Review, we discuss the ceramic manufacturing of solid-state Li-ion conductors into thin films and investigate their chemistry and Li-ion motion for lithionic-device applications, including energy storage in microbatteries, sensors of toxins and greenhouse gases, and neuromorphic computing mimicking human-brain operations (BOX 1). We further highlight promising applications and explore the future of functional Li-ceramic films beyond classic energy storage.

Li ceramics for lithionic devices

Functional ceramics can perform multiple tasks with high efficiency, including energy storage and conversion, neuromorphic information processing, data storage and

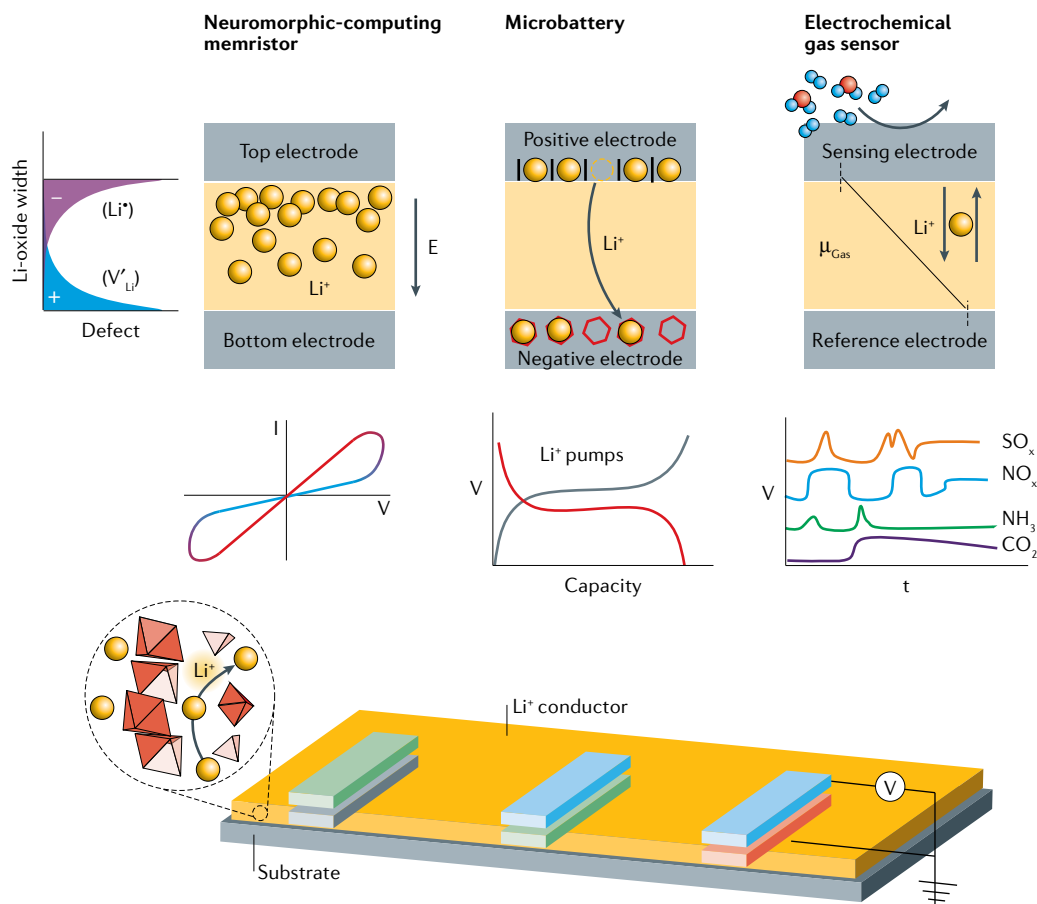
environmental-gas sensing, based only on ion transport within electrochemical-cell arrangements. In addition, the chemistry, electronic structure and ion conduction of functional ceramics, such as O^{2-} , H^+ and Li^+ conductors, can be modified. In this Review, we focus on the repurposing of Li oxides, used in large-scale battery electrochemistry, as thin-film electronic entities for sensing, neuromorphic computing and on-chip energy storage, serving multiple functions in chip architectures and electronic devices (BOX 1).

Compared with traditional semiconducting materials, such as Si, Ge, GaN, GaAs and SiC, used in microelectronic devices, which mainly operate based on the movement of electrons, the electronic states and ionic defects in Li ceramics can be modulated by altering the Li-ion chemistry, for example, by intercalation and deintercalation, conversion and alloying. Therefore, electrochemical devices in the lithionics vision can be operated using only a few Li-oxide films, with the operation principle defined by the electrode sets (BOX 1). In a Li-operated neuromorphic-computing memristor, Li ions are redistributed through the Li-oxide switching layer upon application of an external electric field, resulting in different resistive states across the film. By contrast, in a microbattery, a Li-conductive electrolyte film separates the electrodes, and the Li ions undergo intercalation and deintercalation during charging and discharging. In a (type III potentiometric) electrochemical gas sensor, Li ions are transported through the Li-conductive electrolyte layer when the chemical potentials change between the sensing and reference electrodes; gas concentrations can then be determined by measuring the voltage across the Li-conductive electrolyte. All three device types require the Li ceramics to be designed and processed in thin-film form with precise control of the chemistry (for example, lithium stoichiometry) and microstructure to achieve high device density and functionality. However, Li-based materials have mainly been manufactured as large-scale ceramics thus far, using bulky and microcrystalline Li oxides, targeted for solid-state batteries. The characteristics and properties can be substantially different between solid-state thin films and thick bulk materials, because thin films (with a thickness $<1\ \mu\text{m}$) have a higher volume ratio of grain boundaries to grains compared with bulk materials, leading to different space-charge potentials and local chemistry¹⁰.

Li is a reactive element with light atomic weight and, therefore, Li stoichiometry can be difficult to control in thin films, in particular, during deposition and post-processing at high temperatures, posing a challenge for the processing of Li-based thin-film ceramics. Thus, techniques to control Li stoichiometry, film chemistry and subsequent film properties remain to be optimized to enable full integration of assembly lines for the manufacturing of Li thin-film devices, which may well take a few decades. Indeed, it took two decades from the discovery of lithium phosphorus oxynitride (LiPON) and its application in microbatteries to a thorough understanding of its local structure and conduction path^{11,12}. Similarly, it will take research efforts to understand the processing and structural control of other Li-oxide

Box 1 | Lithionics

Lithionics defines a class of multifunctional, on-chip devices based on Li-ion-conducting thin films. Lithionic devices include microbatteries, memristors, electrochemical gas sensors and other devices that are based on Li-oxide materials combining various functionalities. Functionalities can be achieved by varying electrode and electrolyte materials that define the electrochemistry and by varying the device design to promote Li-ion migration. In lithionics, Li ions serve as the carrier for information and energy storage, binary and neuromorphic computing, and environmental sensing and tracking.



μ_{Gas} , chemical potential of gas species; E, potential; Li⁺, interstitial Li ion; V['], vacancy.

materials, such as Na super ionic conductor (NASICON) and Li garnets in film form.

Different lithionic devices require different material properties for each Li-oxide film component (TABLE 1). For example, Li electrolytes in microbatteries and sensors must possess high ionic conductivity; in addition, electrolytes in microbatteries should be stable against Li metal to increase the operational-voltage window and assure stable cycling and high energy density, which is not required in sensors. Therefore, the material design needs to be tailored to specific lithionic-device applications. In addition, knowledge exchange between solid-state batteries, electrochemical gas sensor and neuromorphic-computing communities will help to overcome manufacturing-related challenges and facilitate innovations in applications and devices.

Solid-state Li-conducting films

Li-oxide-based glasses¹³, Li-sulfide-based glasses^{14,15} and oxysalt-based electrolytes were the first materials explored as Li-conducting solid-state electrolytes¹⁶, followed by the discovery of LiPON^{17,18} (FIG. 1a). Inorganic

solid-state electrolytes have been intensively investigated in Li-ion-battery research, opening up opportunities for direct, on-chip application of thin-film microbatteries. The most studied Li-ion-conducting ceramics are based on LiPON^{19–21}, NASICON-type^{22,23}, perovskite-type^{24–27} and garnet-type structures^{28–31} (FIG. 1a,b); for example, Li(Al,Ti)₂(PO₄)₃ (LATP), Li_{3x}La_{2/3-x/3}TiO₃ (LLTO) and Li₇La₃Zr₂O₁₂ (LLZO).

The transport properties of Li conductors were first mainly investigated in millimetre-sized ceramics, typically processed as pellets, with Li-ion conductivities of 10⁻⁷–10⁻³ S cm⁻¹ at room temperature (FIG. 1c). By contrast, the conductivities of Li-oxide thin films are more than one order of magnitude lower at room temperature (FIG. 1c), with the exception of LiPON thin films, which have a higher conductivity than bulky amorphous LiPON pellets^{19,32}. The reduced conductivity in thin films is often the result of Li loss at high temperatures during deposition or post-annealing³³, which can be addressed by providing extra Li during processing^{33,34}. In addition, size effects are more dominant in microdevices; in particular, the Li-conductor

Table 1 | Li-based material requirements for lithionic devices

Component	Thin-film microbattery	Neuromorphic-computing memristor	Electrochemical gas sensor
Electrode	<p>Positive electrode: high voltage and capacity; good electrochemical and chemical compatibility with the solid-state electrolyte over many cycles; example materials are LiCoO_2, LiMn_2O_4, LiNiMnCoO_2</p> <p>Negative electrode: low voltage and high capacity; uniform charge and discharge; ideally Li metal; example materials are Li metal, $\text{Li}_4\text{Ti}_5\text{O}_{12}$, Si, C</p>	<p>Stable against metallic electrodes at high electric fields</p> <p>Li intercalation at the interfaces</p> <p>Example materials: Pt, Au</p>	<p>Sensing electrode: good thermal and mechanical stability; must be in contact with electrolyte (mobile ions), metal electrode (electrical signal) and targeted gas; example materials are Li_2CO_3 (CO_2 sensor), NaNO_2 (NO_x sensor), Li_2SO_4 (SO_x sensor)</p> <p>Reference electrode: stable to avoid voltage drift in the sensor signal; high conductivity to improve response time; stable at the targeted gas concentrations; example materials are Pt, Au</p>
Electrolyte	<p>High ionic conductivity with low electronic conductivity (transference number, $t_{\text{ion}} \sim 1$)</p> <p>Low toxicity and cost</p> <p>Wide electrochemical-stability window</p> <p>Preferably compatible with Li metal</p> <p>Mechanically robust against Li penetration at high current density</p> <p>Good electrochemical and chemical compatibility with positive and negative electrode</p> <p>Example materials: LiPON, LLTO, LLZO</p>	<p>Availability of metal-to-insulator transition preferred</p> <p>2D or 3D Li conductor</p> <p>Fast resistive switching kinetics</p> <p>Control over retention</p> <p>Long-term stability</p> <p>Phase evolution at high electric fields</p> <p>Example materials: LiCoO_2, $\text{Li}_4\text{Ti}_5\text{O}_{12}$</p>	<p>High ionic conductivity to ensure fast response</p> <p>Inactive (high durability at operating temperature) to the targeted gases</p> <p>Good chemical stability at operation temperature and atmosphere</p> <p>Example materials: LiPON, Li_3PO_4, LLZO</p>

LiPON, lithium phosphorus oxynitride; LLTO, $\text{Li}_{3x}\text{La}_{2/3-x/3}\text{TiO}_3$; LLZO, $\text{Li}_7\text{La}_3\text{Zr}_2\text{O}_{12}$.

Debye length can affect space-charge-layer thickness and may also impact the interfacial charge profile and interphase stability. For example, LLZO has a high doping level to stabilize phases, whereas LLTO has a lower extrinsic doping level and, thus, the Debye length can vary, which may affect the downscaling of lithionic microdevices. However, the exact mechanisms of the impact of size on the space-charge layer in different Li materials remains elusive, in particular, for Li-oxide films. Moreover, electrochemical-stability windows have mainly been investigated in Li ceramic pellets thus far (FIG. 1c); however, they also need to be assessed in thin-film Li conductors, because the stability windows of films and pellets may differ. For example, the electrochemical-stability window of LiPON has been calculated and experimentally demonstrated by cell testing in thin-film form, whereas the stability windows of most other solid electrolytes (for example, LATP, LLTO and LLZO) have only been studied in pellet form thus far. However, stability windows are crucial for determining the choice of electrodes and for defining the key operational performance parameters (that is, energy density in batteries, the resistance ratio between the on and off state ($R_{\text{on/off}}$) in memristive devices and voltage readout in gas sensors).

Ceramic processing offers the opportunity to define the chemistry and understand the relation between structure and Li-ion transport in films, which is important for determining the energy and information density of batteries and for the design of neuromorphic computing and sensing units based on Li. With the exception of LiPON^{35,36}, most thin-film Li conductors have not yet been integrated in microbatteries (of note, LLTO has only been applied in half-cell microbattery structures)²⁷. Interestingly, LiPON-based gas sensing has

been applied about 10 years after its implementation in microbatteries. Similarly, LLTO and LLZO have only been integrated in memristors and gas sensors over the last 10 years (FIG. 1a). This time delay is a result of the difficulties of Li thin-film processing, which often leads to low Li-ion conductivity as compared with bulk pellets. To enable device-level applications, the electrolytes must minimize the conductivity gap between bulk and films. For applications in microbatteries, Li-dendrite resistance and interfacial stability also need to be improved, whereas solid-state sensors have fewer restrictions for materials selection.

Li-controlled electronic configurations

Research on Li-ion batteries has generated a great amount of knowledge on lithiated transition-metal (TM) oxides, which are traditionally used as electrodes in batteries (FIG. 2a). According to their Li-ion migration pathway, these materials can be classified as 1D (olivine) conductors, such as LiFePO_4 (REFS^{37–40}), 2D (layered) conductors, such as LiCoO_2 (REFS^{41–43}), and 3D (spinel) conductors, such as $\text{Li}_4\text{Ti}_5\text{O}_{12}$ (REF.⁴⁴) and $\text{Li}_x\text{Mn}_2\text{O}_4$ (REFS^{45–47}) (FIG. 2a,b). Layered Li conductors have the general formula Li_xMO_2 and are the most widely investigated electrode materials. Li-transport dimensionality needs to be considered for lithionics applications, because the performance depends on the preferred transport orientation. Lithiated TM oxides have long been mass-manufactured in Li-ion batteries, in which bulk-processed ceramics are combined with conductive carbon coatings to mitigate low electronic conductivities. When used in thin-film form, the thickness of the electrode layer needs to be increased to increase the energy density of microbatteries. However, other lithionic applications require the exact opposite,

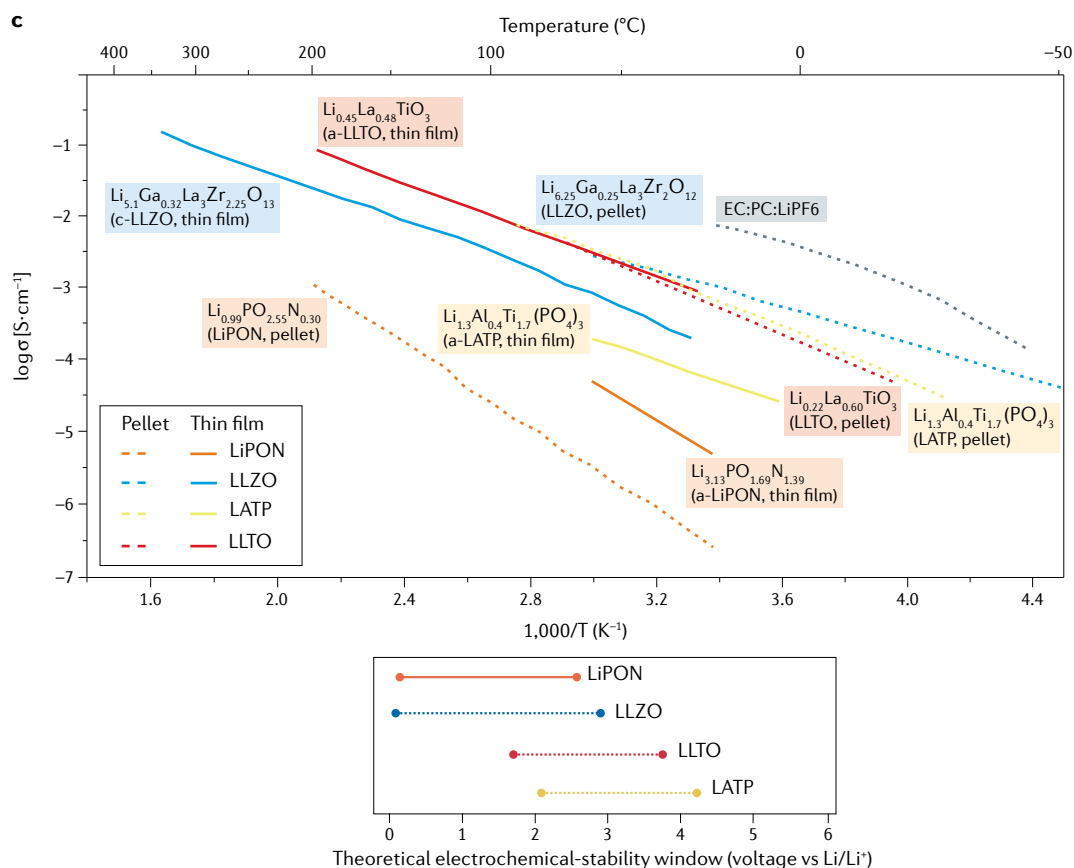
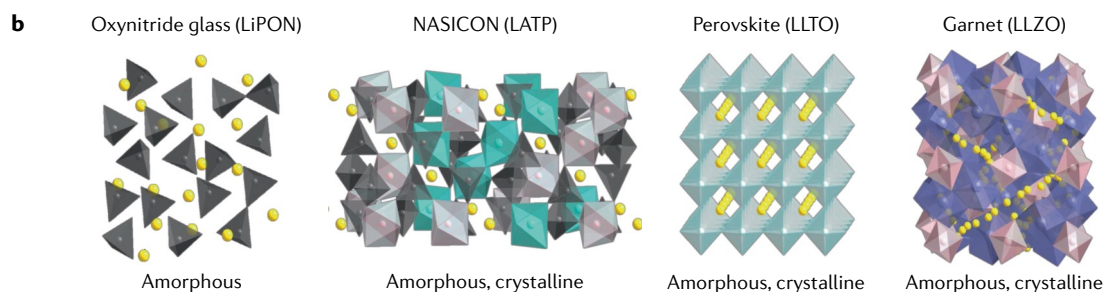
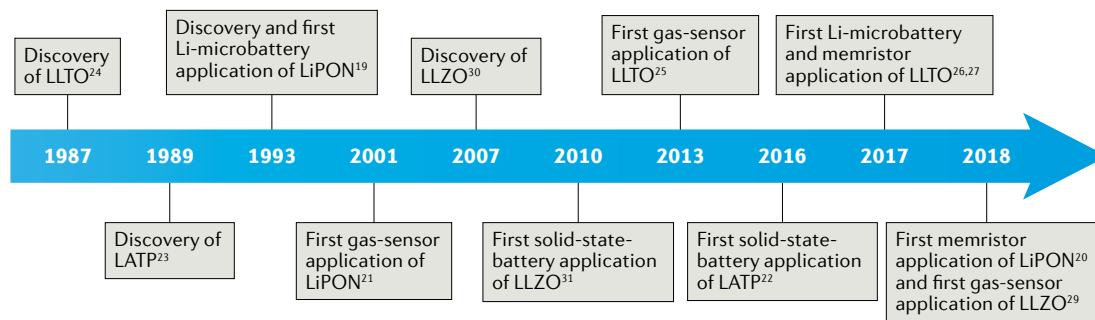
a Discovery timeline of LiPON, LATP, LLTO and LLZO solid electrolytes and their lithionic-device applications


Fig. 1 | **Oxide-based Li-ion conductors.** **a** | Timeline of Li-based solid electrolytes and lithionic-device applications. **b** | Structures and Li-conduction paths of oxide-based Li-ion conductors, including amorphous lithium phosphorus oxynitride (LiPON), Na super ionic conductor (NASICON)-type $Li_{1.3}Al_{0.3}Ti_{1.7}(PO_4)_3$ (LATP), perovskite-type $Li_{3x}La_{2/3-x}TiO_3$ (LLTO) and garnet-type LLZO, $Li_7La_3Zr_2O_{12}$ (LLZO). **c** | Li-ion conductivity of Li-oxide-based solid-state electrolytes in pellet and thin-film form compared with state-of-the-art liquid electrolytes, including the highest reported values of pellet-type and thin-film LLZO^{34,202}, LLTO^{203,204}, LATP^{205,206} and LiPON^{32,155}, and theoretical electrochemical-stability windows based on first-principles thermodynamic calculations²⁰⁷. The processing temperatures are shown for pellets and thin films. The classification as amorphous (or crystalline) thin film or pellet (or tape) are indicated by a- and c-, respectively.

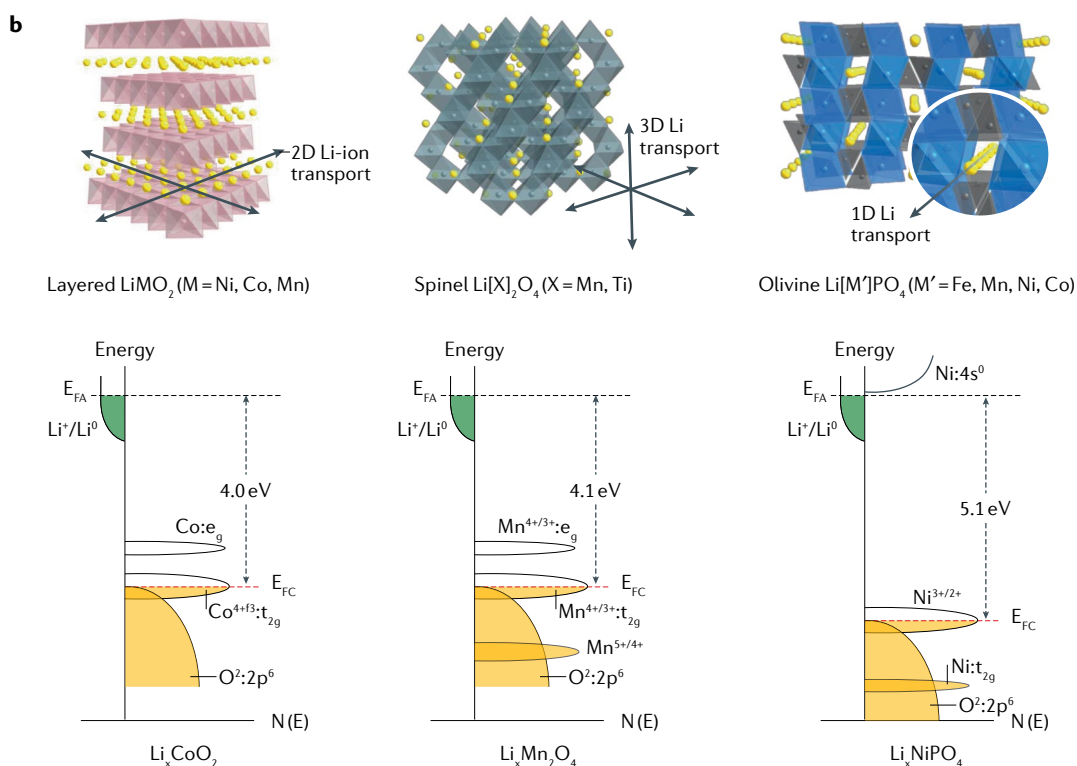
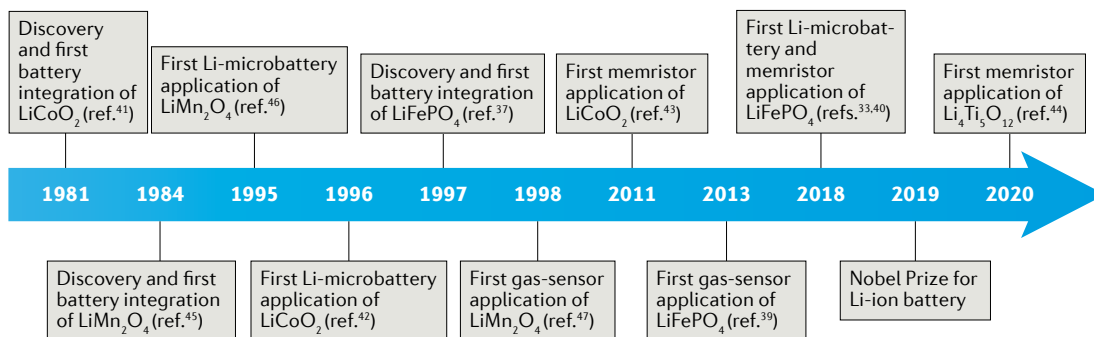
a Discovery timeline of Li-conducting layered, spinel and olivine ceramic films and their lithionic-device applications


Fig. 2 | **Li-controlled electronic configurations.** **a** | Timeline of Li-conducting ceramic films and lithionic-device applications. **b** | The structure, Li-conduction path and band gap of layered-type LiMO_2 , spinel-type $\text{Li[X]}_2\text{O}_4$ and olivine-type Li[M']PO_4 . E_{FA} , Fermi energy of Li anode; E_{FC} , Fermi energy of cathode. Panel **b** adapted from REF.²⁰⁸, CC BY 4.0.

that is, ultra-thin and smooth films, to achieve the high local-electric-field strength that is needed for memristors or to realize fast kinetics and high surface control for sensor chips.

Li intercalation and extraction processes, as well as high electric fields, have a profound effect on the electronic structure of these materials, owing to the valence change in the TM, which can result in a variety of non-linear physico-chemical effects. For example, the metal-insulator transition of Li_xCoO_2 is linked to a first-order structural transformation with phase coexistence between the insulating ($x > 0.95$) and metallic ($x < 0.75$) phases upon deintercalation^{48–50}. Li insertion and extraction kinetics, as well as the associated structural stability and storage capacity, are important for battery performance, whereas electronic-structure changes related to lithiation and the transport

dynamics determined by the ion-pathway dimensionality play a key role in neuromorphic computing based on memristance^{51–53}.

Layered conductors

Layered battery-electrode materials consist of repeated layers of Li and TM ions in a cubic, close-packed structure of oxygen atoms^{54,55} (FIG. 2b); for example, in Li_xCoO_2 , Li and Co cations are octahedral-coordinated and distributed along alternating layers with hexagonal symmetry. In a simplified picture, Li ions deintercalate from the Li-rich layered structure, inducing oxidation of the TM from Co^{3+} to Co^{4+} and expanding the unit cell, which results in a metal-insulator transition with high resistivity change⁵⁰. As a result, layered materials with 2D Li transport can store large amounts of Li and, thus, are popular high-voltage, high-capacity and stable battery

cathodes⁵⁶. LiCoO₂ films have also been applied for neuromorphic computing (FIG. 2a), owing to their memristive behaviour⁴³, enabling operation at low energy per computational operation and cycle⁴³. Redox-based transistors can be operated using Li pumps, which modulate the resistive character and the electronic state of LiCoO₂ (REFS^{57,58}).

Spinel conductors

Li-spinel structures have the formula LiM₂O₄, with M = Ti, Mn, in which Li is tetrahedral-coordinated and the TM is octahedral-coordinated. Upon Li insertion, Li ions fill empty octahedral positions, promoting the formation of the lithiated Li₂M₂O₄ phase⁵⁹ (FIG. 2b). Compared with layered Li oxides, spinels provide a 3D network for Li diffusion at the expense of capacity. In addition, fine control of the lithiation state plays a key role in the modulation of the memristive properties of Li titanate thin films⁴⁴.

Olivine conductors

In olivine structures (LiMPO₄, with M = Fe, Mn, Co or Ni), TM and Li are octahedral-coordinated. The TM, for example, Fe, defines the layers along the *bc* plane and Li is located along octahedral channels, which results in 1D ion-diffusion pathways³⁷ (FIG. 2b). Li intercalation and deintercalation occur via a two-phase equilibrium between the phase polymorphs, LiFePO₄ and FePO₄. Pure and doped LiFePO₄ thin films have been used as functional ceramics for neuromorphic computing and chemical sensing; for example, LiFePO₄ thin films show promising switching speeds below 50 ns for neuromorphic computing³⁸, and sensing applications of LiFePO₄-based thin films were shown for formaldehyde³⁹ and other organic compounds, such as xylene⁶⁰.

Application challenges in thin-film devices

Layered, olivine and spinel Li materials have mainly been optimized for batteries thus far. However, neuromorphic-computing operations based on memristive or Li-modulated transistors and chemical-sensing applications have also been reported. Redox-state changes induced by Li-ion diffusion and reactions, which can be accompanied by metal-insulator transitions, allow the fine control of the electronic configuration, which is important for the implementation of ceramic films in devices. However, challenges remain for Li-driven computation and fast sensing in AI applications, which demand control of the electronic and Li state changes at substantially higher rates (10⁶ Hz) and with greater endurance (10⁶ cycles), as benchmarked by the latest flash memory and silicon-oxide-nitride-oxide-silicon (SONOS) technologies⁶¹, than required for battery-electrode operation (Li-transport rates of approximately 10⁵ Hz for ~10⁵ cycles at best)⁶². In addition, phase evolution and stability, as well as volume expansion, remain to be computed and probed for high electric-field strengths of up to 10⁷ V m⁻¹, as required for Li neuromorphic-computing applications. Similarly, for sensing applications, the response in different gas atmospheres, as well as ion selectivity, transport and catalyst integration, need to be investigated.

Solid-state thin-film batteries

The increasing complexity of portable electronics and personal tracking devices has led to a growing demand for energy-storage solutions with improved gravimetric and volumetric energy density^{63–65}. Current technologies mainly rely on Li-ion batteries with liquid-organic electrolytes, limiting the volumetric energy density of the battery. From an industry perspective, the targeted energy density of next-generation batteries is >500 Wh kg⁻¹ (REF. 66), which is significantly higher than that of state-of-the-art automotive Li-ion batteries (~210 Wh kg⁻¹)⁶⁷, with a target power output density of 2,000–4,000 W l⁻¹ and a pack cost below US\$125 kW h⁻¹ (REF. 66). The replacement of liquid organics with solid-state electrolytes is expected to not only reduce the volume and weight of batteries but to also enable the use of high-capacity anodes (for example, Li metal) and high-voltage cathodes (for example, LiNi_{0.5}Mn_{1.5}O₄ or LiNi_{1/3}Co_{1/3}Mn_{1/3}O₂)^{36,68,69}. Furthermore, solid-state electrolyte films can be used as barriers for Li filament formation. To meet these energy and cost targets, and to compete with liquid-organic electrolytes, mass-manufacturable ceramic-processing techniques need to be developed that are suitable for thin films.

Thin-film battery architectures

The fabrication of Li-oxide solid-state electrolytes by ceramic thin-film processing technologies gave rise to thin-film microbatteries, which are a promising solution for on-chip integrated energy storage with 3D stacking potential and improved safety compared with liquid-electrolyte-based battery packs^{70,71}. Solid-state microbatteries consist of two current collectors and an electrolyte sandwiched between two active electrodes (FIG. 3a). Compared with classic Li-ion batteries, the main difference is that microbatteries use a solid-state ceramic Li-ion conductor instead of an organic liquid and a porous polymer separator. The rate performance of planar microbatteries is generally lower than that of state-of-the-art Li-ion batteries. However, 3D microbatteries with a large interfacial contact area can address this limitation, because they show better charge-transfer efficiency and higher energy and power density owing to higher volumetric mass loading of the active electrode materials^{71,72}.

3D microbattery architectures can be fabricated by additive manufacturing using templates to directly grow shapes, such as pillars or rods, for one of the electrodes, followed by film deposition to add the electrolyte and second electrode. Alternatively, subtractive manufacturing can be applied; for example, etching of channels in the substrate using shadow masking or photolithography, followed by filling of the channels with the microbattery materials. Various 3D microbattery architectures have been fabricated, including 3D microbatteries with nanorods, 3D microbatteries with microchannels and interdigitated 3D battery structures (FIG. 3b–d). Compared with planar batteries, the volumetric loading of the active anode and/or cathode is higher in 3D architectures, leading to improved cycling performance.

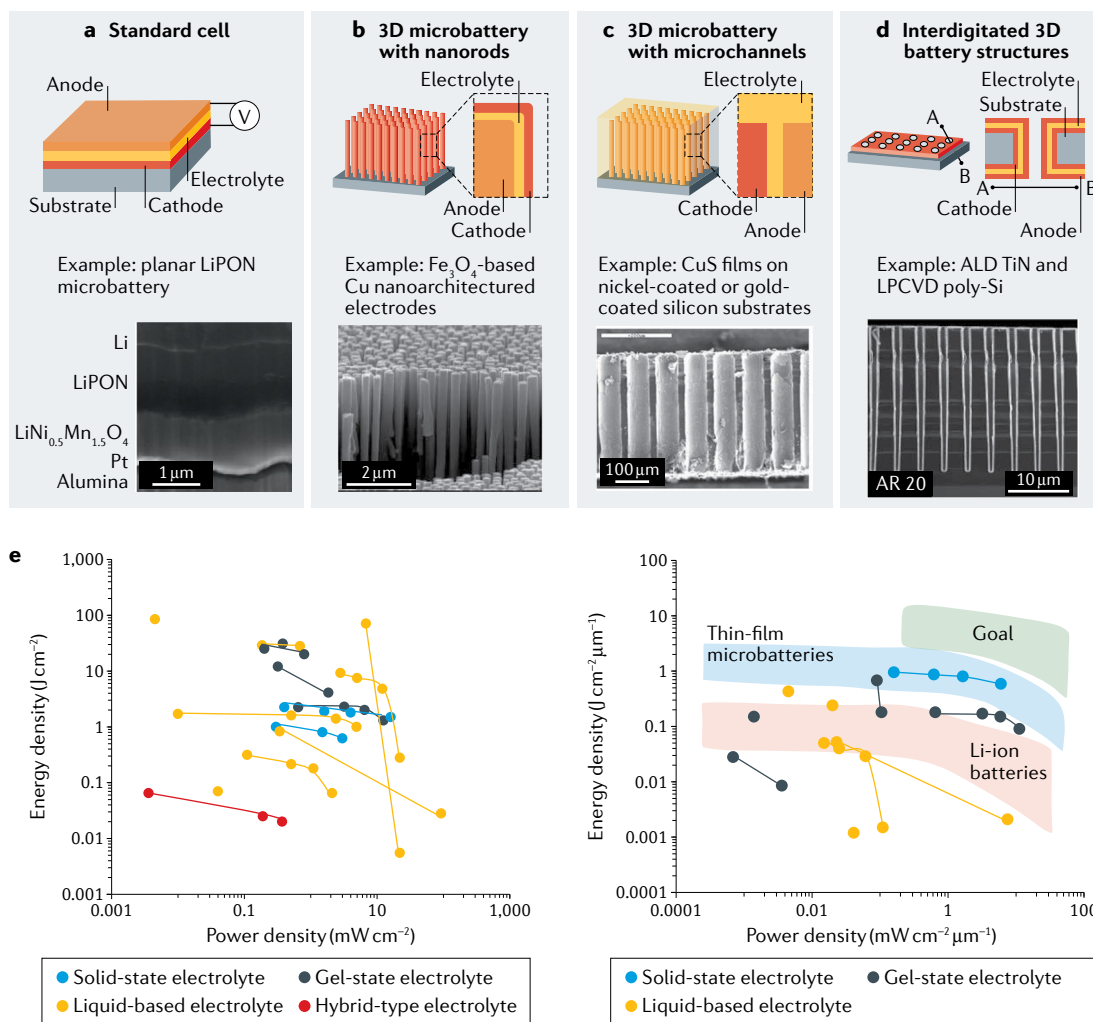


Fig. 3 | **Thin-film solid-state battery designs.** **a** | Standard design of a thin-film solid-state microbattery⁶². **b** | 3D microbattery based on nanorods⁷⁵. **c** | 3D microbattery based on microchannels⁷⁶. **d** | Interdigitated 3D battery⁷⁷. **e** | Energy density versus power density for various state-of-the-art battery systems^{36,73,209–221} (left panel: not standardized by thickness; right panel: standardized by thickness). ALD, atomic layer deposition; LiPON, lithium phosphorus oxynitride; LPCVD, low-pressure chemical vapour deposition. Panel **a** reprinted with permission from REF.⁶², Wiley. Panel **b** reprinted from REF.⁷⁵, Springer Nature Limited. Panel **c** reprinted with permission from REF.⁷⁶, The Electrochemical Society. Panel **d** adapted with permission from REF.⁷⁷, RSC.

3D microbatteries with nanorods. Cu-nanorod current collectors grown by electrolysis can serve as template for the deposition of conversion-type Fe_3O_4 (REFS^{73–75}) (FIG. 3b). The main advantages of this approach are the simple fabrication of 3D electrodes and that the size of the nanorods can be tuned by using template membrane or substrates. However, template-assisted deposition produces substrates with open structures, which can affect the subsequent deposition of the battery layers.

3D microbatteries with microchannels. 3D architectures of thin CuS films on gold-coated or nickel-coated silicon substrates can be fabricated by forming microchannels using electrodeposition⁷⁶ (FIG. 3c). Electrodeposition allows the control of the amount of deposited material, the formation of conformal layers onto 3D porous structures and scalable depositions on large areas.

Interdigitated 3D structures. Interdigitated 3D battery structures rely on the formation of 3D trenches (FIG. 3d). The trenches are etched into polycrystalline Si, followed by low-pressure chemical vapour deposition of TiN, which serves as the current collector and Li barrier layer. Compared with planar battery geometries, the capacity of microbatteries with trench structures is at least five times higher^{77,78}. The main advantage of 3D trenches is the good processing compatibility with Si-based complementary metal–oxide–semiconductor (CMOS) manufacturing.

These 3D architectures permit solid-state diffusion of Li into the electrodes, which improves the kinetics during charging and discharging of microbatteries. Furthermore, macroscopic film techniques, such as biotemplating^{79,80} and 3D printing^{81,82}, could be used in combination with thin-film deposition techniques (vacuum-based or solution-based) to improve the

electrochemical performance of thin-film batteries with a better control of the charge-transfer kinetics at higher charge and discharge rates. However, 3D printing is typically not used for thin films because it requires post-sintering. In addition, details of the structure–performance relationships of 3D microbatteries remain elusive thus far.

Thin-film battery materials

A variety of materials and electrode–electrolyte combinations are theoretically suitable for microbatteries; however, only two solid-state electrolytes have been used for the design of microbatteries thus far^{27,36,62} (TABLE 2). For example, LiPON-based microbatteries show impressive cyclability of up to 10,000 cycles at a rate of C/10 with a Li-metal anode, a $\text{LiNi}_{0.5}\text{Mn}_{1.5}\text{O}_4$ cathode and a LiPON electrolyte film (thickness of 1–2 μm)⁶². In this microbattery, a planar cell is deposited on an alumina substrate, and the cathode and electrolyte films are fabricated by radio frequency magnetron sputtering⁶². The good rate performance demonstrates the potential of LiPON as a solid-state electrolyte, which has already been commercialized.

Microbatteries based on perovskite-structured LLTO solid electrolytes have not yet reached the maturity of LiPON-based microbatteries (TABLE 2). For example, amorphous LLTO films can be deposited by pulsed laser deposition onto $\text{LiNi}_{0.5}\text{Mn}_{1.5}\text{O}_4$ to form a half-cell, which maintains 98% capacity retention for 50 cycles up to 4.8 V (REF.²⁷). Nevertheless, to the best of our knowledge, thin-film microbatteries with Li-garnet-based or NASICON-based electrolytes have not yet been developed, possibly owing to the fact that the high conductivity of these materials in film form has only recently been reported³³.

The interplay between high current density ($>1 \text{ mA cm}^{-2}$) and safety is an important consideration for microbatteries. Cycling at high current densities would enable faster charge and discharge, facilitating new applications of microbatteries in lithionic devices, for example, three-terminal memristive devices. However, nucleation and growth of Li dendrites can occur in solid electrolytes, including in poly-crystal and single-crystal garnet-type LLZO and amorphous sulfide⁸³. Grain boundaries are susceptible to Li dendrites and facilitate their intergranular propagation through the solid electrolyte (demonstrated in bulky pellet tests) at low current densities⁸⁴. By contrast, in amorphous LiPON, Li deposition is confined to an artificial LiPON–LiPON interface

(prepared by radio frequency magnetron sputtering), which is located parallel to a LiCoO_2 cathode⁸⁵. The confinement of Li dendrites to the LiPON–LiPON interface suggests that the homogeneous, grain-boundary-free morphology of amorphous LiPON is crucial for the blocking of Li-dendrite growth, even at high current density (that is, 10 mA cm^{-2})^{36,86}. Other amorphous Li-oxide films, for example, amorphous LLZO⁸⁷ and amorphous LLTO^{88,89}, could also be integrated into microbatteries, which will require a thorough investigation of the electrode–electrolyte interface to establish the electro-chemo-mechanics and to develop microbatteries with high volumetric energy density. To overcome dendrite growth in microbatteries, grain-boundary chemistry and interparticle structures could be modified to improve the mechanical strength, toughness and elastic modulus of the solid-state electrolyte. In addition, the strains at the interfaces in microbatteries, which can be induced by lattice mismatch or by the substrate, need to be analysed in detail. Finally, fully amorphous and defect-free Li-oxide electrolytes with high Li-ion conductivities could be developed to minimize non-uniform current densities and to prevent dendrite propagation; the band gap, surface chemistry and transference number of the electrolyte need to be considered to engineer barriers for Li dendrites.

Power and energy density

Cyclability of up to 10,000 cycles has been demonstrated for state-of-the-art microbatteries with a Li-metal anode; however, cyclability at high current densities ($>1 \text{ mA cm}^{-2}$) needs to be achieved to enable their application in lithionic devices. The energy and power densities of microbatteries can vary by nearly five orders or magnitude per unit area (FIG. 3e). The highest power density (30 mW cm^{-2}) has been reported for LiPON-based microbatteries⁸⁶. Therefore, a common research goal is to increase the power and energy densities of Li-metal batteries to $>1 \text{ mW cm}^{-2} \mu\text{m}^{-1}$ and $>1 \text{ J cm}^{-2} \mu\text{m}^{-1}$, respectively (FIG. 3e), which requires the transformation of conductors from pellet or tape form to thin-film form to produce thin-film solid-state electrolytes with high Li-ion conductivity ($>10^{-5} \text{ S cm}^{-1}$ at room temperature) coupled with 3D architecture electrodes. Indeed, integrating amorphous solid electrolytes directly into 3D microbatteries would increase the power and/or energy densities of the entire cell; however, the electrode–electrolyte interfacial compatibility needs to be thoroughly investigated and the interfacial resistance reduced.

Table 2 | Li-oxide-based all-solid-state thin-film batteries

Material			Deposition method			Capacity (mAh g^{-1})	Cycling number	Ref.
Electrolyte	Cathode	Anode	Electrolyte	Cathode	Anode			
LiPON	LiCoO_2	Li metal	RF sputtering	RF sputtering	Thermal evaporation	137	4,000	36
		$\text{LiNi}_{0.5}\text{Mn}_{1.5}\text{O}_4$	Li metal	RF sputtering	RF sputtering	Thermal evaporation	122	10,000
Perovskite (amorphous LLTO)	$\text{LiNi}_{0.5}\text{Mn}_{1.5}\text{O}_4$	$\text{LiNi}_{0.5}\text{Mn}_{1.5}\text{O}_4$	PLD	PLD	PLD	–	50	27

LiPON, lithium phosphorus oxynitride; LLTO, $\text{Li}_{1-x}\text{La}_{2/3-x}\text{TiO}_3$; PLD, pulsed laser deposition; RF, radio frequency.

The interfacial reaction, which can extend up to 100 nm and adversely affect battery performance⁹⁰, can be prevented by applying an interfacial barrier layer between the electrode and the electrolyte (as thin as 5 nm)⁹¹.

Thin-film processing enables the integration of different thin-film Li conductors into microbatteries and more precise tuning of grain-boundary chemistry and structure as compared with sintered ceramics; however, the chemistry at grain boundaries needs to be resolved at the atomic scale. Faster charging and discharging rates as well as higher volumetric and gravimetric energy densities will be achieved in solid-state microbatteries by capitalizing on the advances in Li thin-film-conductor fabrication as solid-state electrolytes with higher Li-ion conductivities (for example, thin-film Li garnets), as well as by designing batteries with porous electrodes enabling low interfacial resistance and high loadings of high-voltage cathodes^{92,93}.

Neuromorphic computing with Li

The integration of novel computing schemes and the implementation of AI at the hardware level require innovative materials and novel device solid-state ionic chemistry^{94,95} (FIG. 4a). Neuromorphic computing mimics the basic components of the brain (synapses and neurons); however, digital CMOS technology is not well suited to emulate the analogue responses of the brain⁹⁶. The power consumption of the human brain is approximately 20 W and, thus, for routine tasks, such as image recognition, supercomputers generally consume 10⁵–10⁶ more energy than the human brain⁹⁴. In the brain, memory and processing are interlinked, which is not the case for von Neumann architectures⁶, in which memory and processing units are physically separated. In addition, transistors, which are the main component of von Neumann architectures, are limited by their volatility, difficult miniaturization below 10 nm and difficult integration in 3D designs. Alternatively, memristor^{97,98} arrays enable the application of a variety of neural-network architectures emulating brain functions⁹⁷, owing to their in-memory computing capabilities⁹⁸ (FIG. 4b); for example, deep neural networks (DNNs), in which information is encoded as updated synaptic weights, and spiking neural networks (SNNs), in which information is encoded in the timing and frequency of spikes⁹⁷.

Since the prediction of the memristor⁹⁹ in 1971, its implementation has been widely explored^{53,100–102} and prototype devices are already on the market (*Memristors to Machine Intelligence*). Memristors are now applied in a variety of applications, including resistive random-access memory (ReRAM) for information storage^{103,104}, neuromorphic computing^{105,106} and reconfigurable processing units^{107,108}. The memristor can be considered a non-volatile electrochemical resistance switch, characterized by a hysteretic current–voltage profile, which depends on the polarity, time range and amplitude of the applied voltage⁵³. The defect chemistry of the oxide film and, in particular, ionic and electronic carrier diffusion and distribution at the interfaces determine the switching speed, retention and pulse-symmetry characteristics. Memristors¹⁰⁸ have a great potential for applications in neuromorphic computing in AI owing

to their adaptable properties, including tunable timescales of their fast switching (<sub-nanosecond)¹⁰⁹ and non-volatility for up to 10 years¹¹⁰, combined with high scalability <2 nm at low power dissipation^{97,111}. The versatility of performance and structure makes the memristor a strong competitor to displace electron-based computation schemes using ionic-based in-memory computing.

Valence change and electrochemical metallization memristors

O²⁻, Ag⁺ and Cu²⁺ have been explored for resistive switching in non-volatile memories^{53,102,112}. Oxygen vacancies can act as the main carrier in valence-change memristors⁵³. The resistance change is mainly induced by the motion of oxygen anions (through vacancies) in the solid-state electrolyte, providing large retention but requiring a high switching voltage or current owing to the large diffusion barrier for oxygen; for example, in SrTiO₃ systems, the typical oxygen diffusion coefficient is $D = 10^{-13} \text{ cm}^2 \text{ s}^{-1}$ (REF.¹¹³).

Electrochemical metallization¹¹⁴ systems are based on electrochemically active metal electrodes, such as Ag or Cu, whose highly mobile cations are transported through the solid electrolyte (oxides or other chalcogenides). The low diffusion barrier and large diffusion coefficient ($D = 10^{-4} - 10^{-7} \text{ cm}^2 \text{ s}^{-1}$) of these metallic species lead to low switching currents and voltages in commonly used solid electrolytes, such as Ge_xS_y, SiO₂, Cu₂S (REFS^{115,116}) and also pose challenges in terms of stabilization of resistance states, which lowers the retention performance.

Valence-change memristors have larger retentions than electrochemical metallization systems, which benefits long-term operation of neural networks at the expense of large energy barriers for switching between resistive states. Both technologies further rely on the formation and rupture of ionic filaments as the main mechanism controlling the spatial conductivity of the devices. The stochastic nature of filament formation and rupture is a high-energy-consumption process, inducing non-symmetric switching profiles, which limits the accuracy and efficiency of the neural networks (FIG. 4c,d). However, some valence-change memristors exhibit an area-dependent behaviour, which increases symmetry at the costs of high energy and low switching speeds. Therefore, it remains challenging to implement fast and accurate two-terminal neuromorphic-computing hardware that matches the energy efficiency of the human brain using state-of-the-art memristor technologies. Thus far, neural networks have been realized for small array sizes⁹⁷; for example, face-recognition applications using a DNN 128 × 8 array of HfAl_xO_x/TaO_x devices¹¹⁷. SNNs are even more promising, owing to their predicted low energy consumption; for example, the recognition of spatio-temporal patterns using Si-doped HfO_x memristive units¹¹⁸.

Li-oxide materials for memristors

Li-intercalation materials can address some of the challenges of memristive structures for neuromorphic computing¹¹⁹. These materials have at least two orders

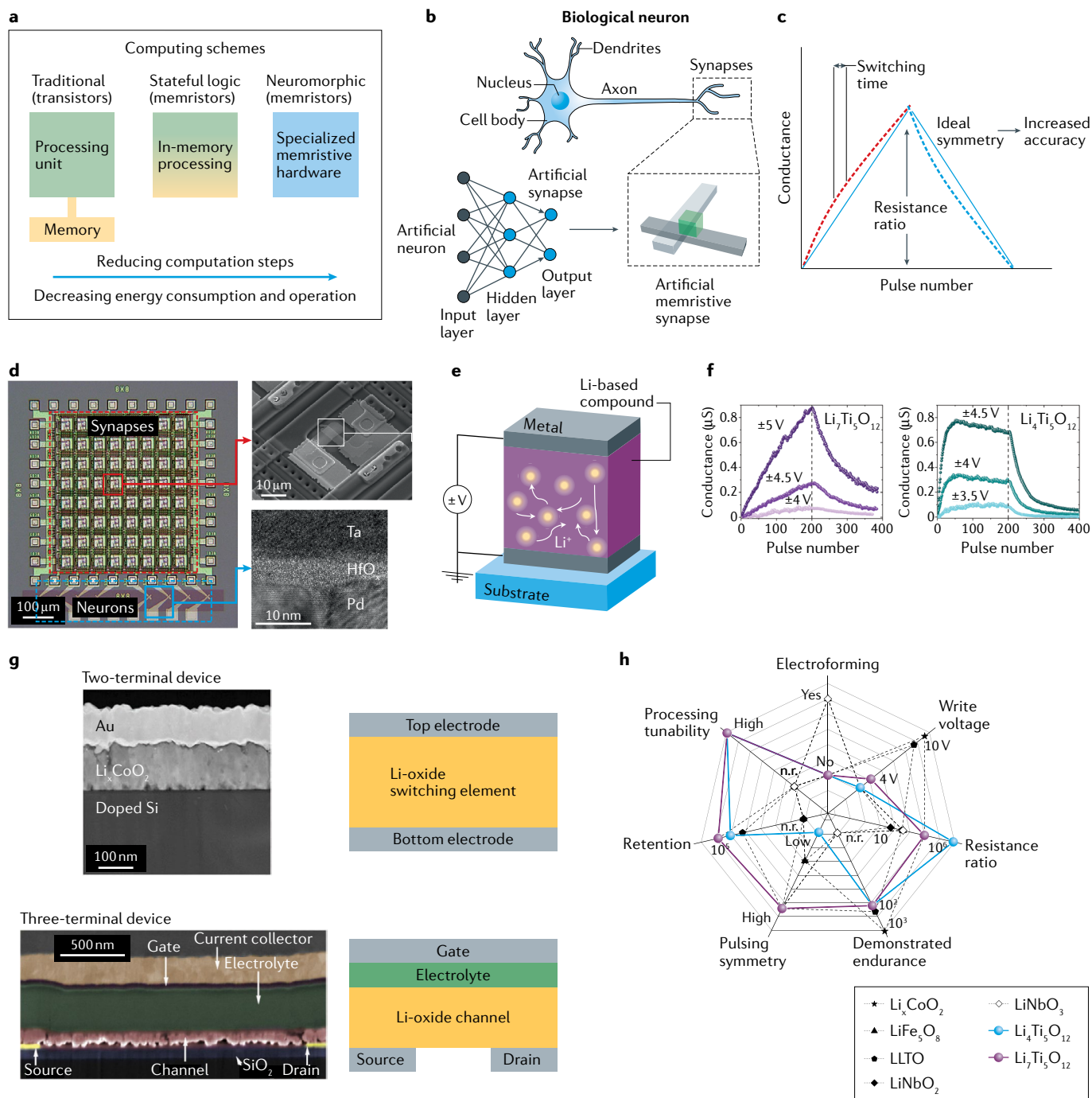


Fig. 4 | Neuromorphic computing with Li-based memristors. **a** | Computing schemes of conventional computing based on transistors and of neuromorphic computing based on memristors. **b** | Neuromorphic computing aims at mimicking human-brain operations using artificial neural networks, in which the weighted connections between neurons consist of memristors. **c** | Main parameters in memristive synaptic weight update. The synaptic performance and accuracy are improved at fast switching times, large resistance ratios and symmetric potentiation and depression operations. **d** | Artificial neural network based on memristors²²². **e** | Two-terminal Li-based memristive device. **f** | Synaptic weight updates by voltage-dependent 500-ms pulses in Li_{4+3x}Ti₅O₁₂ for high Li content (left) and low Li content⁴⁴ (right). **g** | Two-terminal⁴⁴ and three-terminal⁵⁷ Li-based memristive device. **h** | Properties of state-of-the-art Li memristors⁴⁴. LLTO, Li_{3x}La_{2/3-x/3}TiO₃; n.r., not reported. Panel **d** adapted from REF.²²², Springer Nature Limited. Panels **f** and **g** reprinted with permission from REF.⁴⁴, Wiley. Panel **h** adapted with permission from REFS^{57,125}, Wiley.

of magnitude larger diffusivities than valence-change memristors ($D = 10^{-9} - 10^{-11} \text{ cm}^2 \text{ s}^{-1}$)¹²⁰⁻¹²². In addition, Li oxides can undergo large changes in their electronic configuration via metal-insulator transition and phase transitions by adjusting the Li content of the

switching layer⁵⁰. Li-based neuromorphic-computing memristive structures have been developed using traditional battery-electrode materials⁴³ (TABLE 3), for example, high-voltage cathode materials, layered LiCoO₂ (REFS^{43,57,123-125}) Li conductors, such as LiNbO_x

Table 3 | Two-terminal and three-terminal Li-based memristive devices

Lattice dimensionality	Switching material	Metal–insulator transition	Top electrode	Bottom electrode	$V_{\text{threshold}}$	$R_{\text{on/off}}$	Switching mechanism	Film-processing method	Phase evolution probed upon switching	Ref.				
1D	LiFePO ₄	No	Graphite	Au	3 V	~100	Li migration and exchange with electrode	PLD	Yes	38				
2D	LiCoO ₂	Yes	Au	p-Type Si	–4 V	10 ²	Li migration and exchange with electrode	Sputtering	No	199				
			Au	p-Type Si	–3 V, +2.5 V	10 ⁴ –10 ⁵	Li migration and exchange with electrode	Sputtering	No	43				
			Au	p-Type Si	–8 V	10 ⁴	Li migration and exchange with electrode	Sputtering	No	124				
			Pt	Pt	–0.5 V, 1.5–2 V	–	Li migration and exchange with electrode	PLD	No	123				
			Pt (source)	Pt (drain)	–4.1 V to –3.0 V	–	Li migration and exchange with electrode	Sputtering	No	57				
			Pt	SiO ₂ /Si	–2.6 V–7 V	10 ³ –10 ⁴	Li migration and exchange with electrode	PLD	–	134				
	LiNbO _x	No	Pt	Pt	–2.4 V, 1.5 V–2.2 V	180	Non-filamentary and spatially homogeneous	PLD	–	200				
							Pt/Ti	Pt/Ti	–2.8 V, 2.4 V	100	Non-filamentary and spatially homogeneous	PLD	No	129
							Ni/Au	Ni/Au	–8 V, 8 V	1.4–1.5	–	Molecular beam epitaxy	Yes	126
							Pt/Ti	Pt/Ti	>10 V, 2 V	80	Filamentary	Exfoliated from bulk	No	201
3D	LLTO	No	Pt	Pt	1 V, 4 V	10–15	Li migration and polaron hopping	Spin coating	No	26				
	LiPON	No	Au	TiN	–35 V, 11 V	–	Filament formation	Sputtering	Yes	20				
	LiFe ₅ O ₈	Yes	Pt	SrRuO ₃	3 V	150	Filament formation	PLD	No	131				
	Li _{4+3x} Ti ₅ O ₁₂	Yes	Pt	Pt	2–4 V	10 ² –10 ⁴	Electric-field-driven phase separation	PLD	Yes	44				

LiPON, lithium phosphorus oxynitride; LLTO, Li_{3x}La_{2/3-x/3}TiO₃; PLD, pulsed laser deposition.

(REFS^{126–130}), LLTO²⁶ and LiPON²⁰, and the spinels LiFe₅O₈ (REF.¹³¹) and Li_{4+3x}Ti₅O₁₂ (REF.⁴⁴). Depending on the device architecture, 1D (olivine), 2D (layered) or 3D (spinel) Li-ion channels can be used with different Li-concentration-dependent properties, including metal–insulator transitions, phase-separation phenomena and volume expansion. The Li-ion-channel design affects neuromorphic switching performance and allows implementation in two-terminal and three-terminal devices (TABLE 3). Electric-field-induced phase separation on materials with variable electric permittivity and conductivity has been theoretically predicted as a tool

to manipulate memristive behaviour¹³²; for example, to explain the switching behaviour in Li_{4+3x}Ti₅O₁₂ devices⁴⁴.

Li-based memristive devices

Various switching mechanisms have been observed in two-terminal systems (FIG. 4e), including filament-like^{127,131} and more homogeneous mechanisms^{26,125,131,133} (TABLE 3). For example, in devices based on a Li_xCoO₂ layered compound, an exchange mechanism with a Si electrode has been reported^{43,134}, which is uncontrolled and stochastic, and, thus, requires further investigation to reduce switching variability and voltage, and to

increase switching speed. Layered materials with 2D Li migration pathways may be limited by their highly oriented ionic transport; however, Li_xCoO_2 -based resistive switching certainly sparked the interest in Li-based memristive devices. In $\text{Li}_{4+3x}\text{Ti}_5\text{O}_{12}$ — a classic battery anode — Li-concentration-dependent permittivity and the intrinsic miscibility gap between the insulating $\text{Li}_4\text{Ti}_5\text{O}_{12}$ and the metallic $\text{Li}_7\text{Ti}_5\text{O}_{12}$ phases enable local phase separation triggered by a shift in the spinodal and binodal decomposition points under bias, which, in turn, controls the spatial average conductivity of the devices⁴⁴. By controlling the lithiation degree during film processing, the dynamics and magnitude of the phase separation, and, thus, the performance, can be controlled. For example, devices with a stoichiometry close to $\text{Li}_7\text{Ti}_5\text{O}_{12}$ exhibit a symmetric and faster switching behaviour than devices with a stoichiometry close to $\text{Li}_4\text{Ti}_5\text{O}_{12}$, in which asymmetry dominates the switching of the memristor (FIG. 4f). Interestingly, this phase-separation mechanism in Li titanates allows control of the switching symmetry and kinetics in a single material simply by controlling the initial Li stoichiometry, which is unique among materials known for memristors⁴⁴. This behaviour is also relevant for the implementation of two-terminal architectures in neural networks, such as DNNs, in which large retentions and high symmetries are required, and SNNs, in which short retention and large resistance changes are needed.

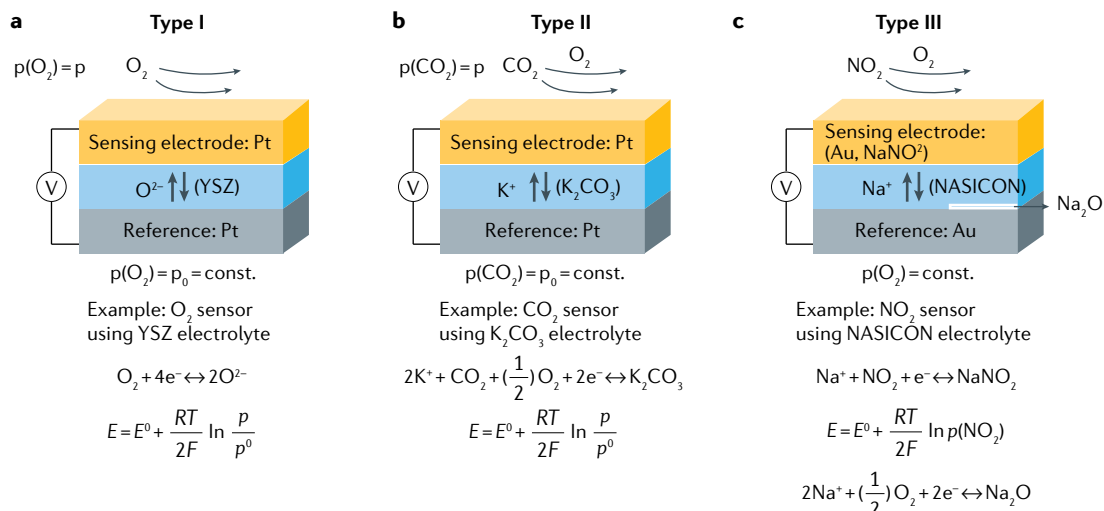
Three-terminal Li-intercalation devices^{57,119,135} can be described (in analogy to a metal–oxide–semiconductor field-effect transistor (MOSFET)) with the two-terminal in-plane electrode–switching oxide–electrode structure as the switching unit (that is, the source and drain contacts in a MOSFET) and the gate on top as a Li pump and source, such as in a microbattery (that is, the gate contact controlling the flux of Li)¹¹⁹ (FIG. 4g). A small bias induces the insertion of Li through a ‘gate-type’ Li electrolyte, and, with a Li source electrode, this leads to a change of the Li stoichiometry of the switching oxide. For example, the Li-ion synaptic transistor for analogue computation (LISTA)⁵⁷ is based on the intercalation of Li-ion dopants into 2D Li-conducting $\text{Li}_{1-x}\text{CoO}_2$ through a LiPON electrolyte and with Si as the Li reservoir (FIG. 4h). This proof-of-principle Li-intercalation device is predicted to operate at 1–10 aJ (REF.⁵⁷), demonstrating that Li-ion-based electronics could match the energy efficiency of the brain with a performance better than that of any other device reported for neuromorphic computation. Indeed, lower energies are required to homogeneously intercalate Li ions compared with O ions, which require higher energies and which are normally geometrically localized in a filament. In theory⁵⁸, 2D in-plane diffusion limits ion transport across the layers of Li_xCoO_2 , causing mechanical strain that relaxes with time, which can affect retention. Alternatively, other fast Li-conductor thin films, such as Li-garnet films³³, could be used instead of LiPON, which may achieve faster switching speeds when integrated as Li-pump gates in three-terminal devices.

Therefore, Li-based materials have a great potential as memristive devices for neuromorphic computing (FIG. 4h). The analogue-like response of Li memristors is more suitable for mimicking brain functions and has higher network accuracy compared with filamentary-operated

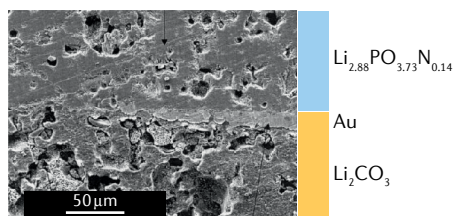
valence change and electrochemical metallization memristors, albeit not yet the same maturity. Knowledge gained from decades of battery research enable the a priori design of materials with ideal structures and transport characteristics for neuromorphic-computing devices. For example, depending on the device architecture, 1D (olivine), 2D (layered) or 3D (spinel) ion channels can be fabricated and their properties can be tuned. However, processing challenges remain in terms of CMOS compatibility, for example, to maintain a desired Li stoichiometry and phases for conductors at low temperatures, and to control its interfaces. Barrier and capsule layers with good chemical and thermal stability need to be developed to mitigate adverse effects related to Li loss and interfacial diffusion. Indeed, a TiN barrier layer with 10-nm thickness can effectively block Li diffusion to Si substrates in planar and 3D device designs, demonstrating the potential of CMOS-compatible processing for lithionic devices¹³⁶. Using Li as the central element of switching enables the tuning of transport and switching characteristics, owing to the rich phase diagram of Li conductors. However, advances in Li-based memristors will depend on the knowledge transfer and collaboration of different scientific communities in industry and academia.

Solid-state electrochemical sensors

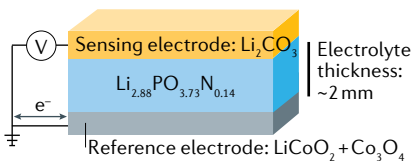
Severe air pollution and emission of greenhouse gases in major cities around the globe caused by human and industrial activities^{137,138} has accelerated the irreversible melting of Antarctic glaciers, triggering a rapid rise in sea levels^{139–141}. Therefore, there is an increasing interest and need for monitoring gas-phase chemicals, such as carbon oxides (CO_x), sulfur oxides (SO_x), nitrogen oxides (NO_x), ozone and volatile organic compounds. The commercial small-gas-sensor market for monitoring ambient gas is segmented by technology, that is, resistive (semiconductor metal oxide) sensors, electrochemical sensors, dispersive infrared radiation absorption and photoionization detection sensors. Solid-state electrochemical gas sensors are not as sensitive as resistive sensors but offer higher selectivity and stability, making them suitable for the sensing of multiple gas species¹⁴². Furthermore, solid-state electrochemical gas sensors do not require as high maintenance as photoionization sensors, which need periodic calibration and lamp replacement^{142,143}. In addition, they are available for a wide range of gas chemicals, as compared with infrared radiation absorption sensors, which show water–vapour and multi-gas interference^{142–144}. Moreover, electrochemical sensors have the potential for miniaturization from ceramic-pellet and thick-film components to on-chip devices using functional thin films as sensor components^{144–147}. Solid-state electrochemical gas sensors can be divided into three classes based on their operating principle and their specific input and output sensing signals: potentiometric, impedancemetric and amperometric gas sensors. As opposed to amperometric sensors, potentiometric gas sensors operate under thermodynamic principles and are independent of device geometry, obviating the need for complicated electronics and making them cost-effective and suited for a variety of applications.



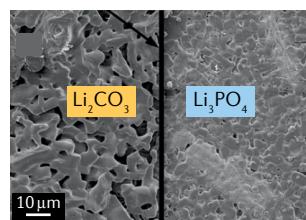
d Pellet-based potentiometric CO_2 sensor



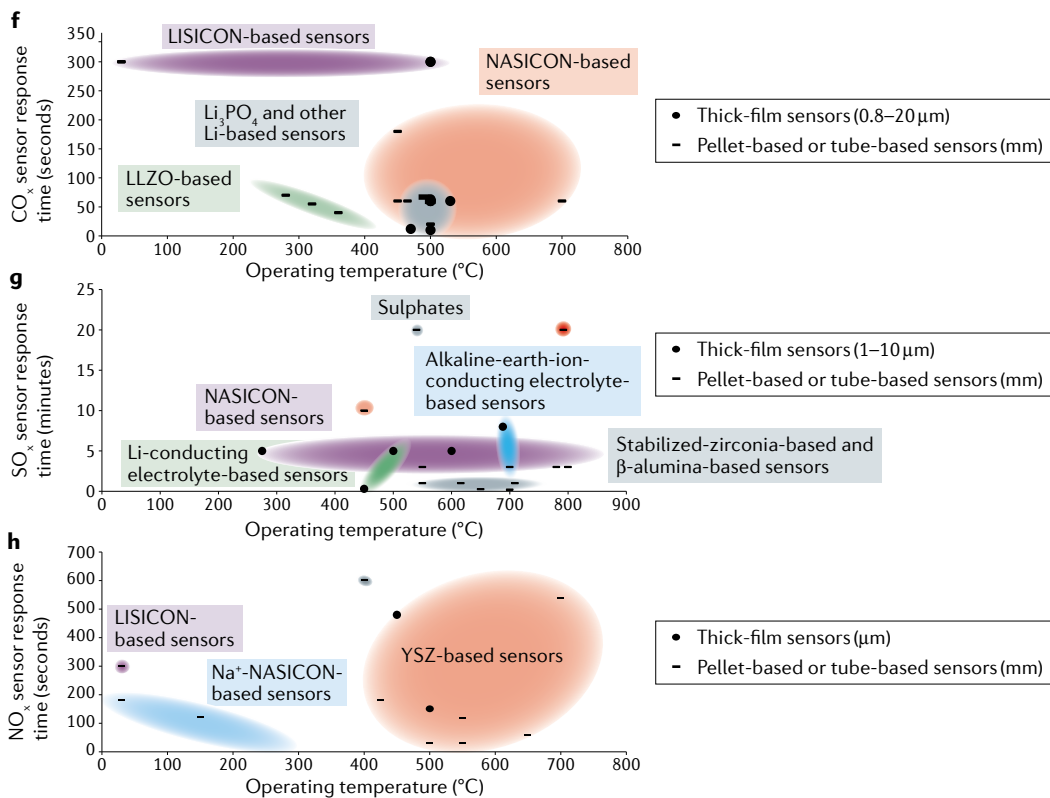
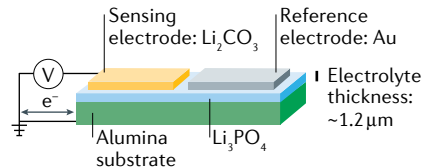
Example: potentiometric CO_2 gas sensor with $\text{Li}_{2.88}\text{PO}_{3.73}\text{N}_{0.14}$ electrolyte



e Thick-film-based potentiometric CO_2 sensor



Example: potentiometric CO_2 gas sensor with Li_3PO_4 electrolyte



◀ Fig. 5 | **Solid-state electrochemical gas sensors.** Electrochemical gas sensors based on Weppner's classification¹⁴⁹. **a** | Type I solid-state electrochemical gas sensors operate by direct measurement of mobile ions in the solid electrolyte. **b** | Type II solid-state electrochemical gas sensors operate by indirect measurement of immobile ions in the solid electrolyte. **c** | Type III solid-state electrochemical gas sensors operate by analysis of other ion species through auxiliary solid phases. **d** | Type III pellet-based CO₂ potentiodynamic sensor with a lithium phosphorus oxynitride (LiPON) electrolyte and Li₂CO₃ as the sensing electrode²¹. **e** | Type III CO₂ potentiodynamic sensor with a Li₃PO₄ thick-film electrolyte and Li₂CO₃ as the sensing electrode¹⁵⁴. **f** | Comparison of sensor response time and operating temperature of Li-conductor-based solid-state CO₂ sensors, including Na super ionic conductor (NASICON)-based sensors^{168–175}, Li super ionic conductor (LISICON)-based sensors^{158,159}, Li₇La₃Zr₂O₁₂ (LLZO)-based sensors⁴⁹, Li₃PO₄-based sensors^{154,160–164}, garnet-type Li₆BaLa₂Ta₂O₁₂-based sensors¹⁶⁵, Li_{3-x}La_{2/3-x/3}TiO₃ (LLTO)-based sensor²⁵ and LiPON-based sensors²¹. **g** | Comparison of sensor response time and operating temperature of state-of-the-art solid-state potentiometric SO_x sensors, including sensors based on stabilized zirconia^{182,183}, NASICON^{153,184,185,223,224}, β"-alumina^{186–189,225}, sulfates²²⁶, alkaline-ion-conducting electrolytes^{190,191} and Li-conducting electrolyte-based sensors^{227,228}. **h** | Comparison of sensor response time and operating temperature of state-of-the-art solid-state potentiometric NO_x sensors, including LISICON-based sensors¹⁵⁹, zirconia-based sensors^{193,229–234} and NASICON-based sensors^{197,198,235}. YSZ, yttria-stabilized zirconia. Panel **d** reprinted with permission from REF.²¹, Elsevier. Panel **e** reprinted with permission from REF.¹⁵⁴, Elsevier.

Potentiometric gas sensors

Potentiometric gas sensors are composed of an electrochemical cell with a sensing electrode (SE), a solid electrolyte and a reference electrode. Derived from the Nernst equation¹⁴⁸, the difference in the chemical potential and different partial pressures at the two electrodes define the electromotive force of the gas sensor, characterizing the voltage of the cell. Depending on the ionic species of the gas, potentiometric gas sensors can be classified into type I (mobile ions), type II (immobile ions) or type III (neither mobile nor immobile ions)¹⁴⁹.

In type I sensors, the detected gas species reacts with the solid electrolyte at the gas–SE–electrolyte triple phase boundary, and is then converted into a mobile ion in the solid electrolyte¹⁴⁹ (FIG. 5a). Type I sensors are typically used as O₂ sensors¹⁵⁰, for example, in automobile exhausts with a zirconium-dioxide electrolyte and porous platinum electrodes. However, these sensors are not commonly used for complex gases composed of multiple elements, owing to a lack of solid-state electrolytes that can conduct complex and often immobile gas species in the solid state¹⁴⁶. By contrast, type II sensors (FIG. 5b) enable the detection of more complex gas species, such as CO₂, NO_x and SO_x, because the gas species is identical to the immobile ions in the electrolyte. Unlike in type I sensors, in type II sensors, ions different from the gas-phase species have sufficient mobility to conduct in the solid electrolyte^{151,152}. From an electrochemical cell-design perspective, both type I and type II sensors require separate gas environments for the SE and reference electrode, which makes their integration into commercial applications more complex¹⁴⁷. In type III sensors (FIG. 5c), an auxiliary phase is used for the SE, which contains both the gaseous ions and the mobile ions from the solid electrolyte^{29,146,147}. Type III sensors offer high sensitivity independent of size, but they rely on the number of triple-phase-boundary reactive sites in the auxiliary electrode. Compared with type I sensors, type III sensors also allow the detection of complex gas species, such as CO₂, NO_x and SO_x (REFS^{29,153}). Moreover, owing to the presence of an auxiliary phase, the selection of mobile and immobile ions for the solid electrolyte is

not restricted as in type II sensors, which opens the door for fast ions, such as Na⁺ or Li⁺, and for as yet unexplored material combinations for sensing devices operating at low temperatures.

Type III gas sensors

Solid electrolytes for type III sensors must provide high ionic conductance to ensure a fast sensing response with high thermal and chemical stability for the detection of a specific gas. Type I solid-state gas sensors require a high operating temperature (>600–1,000 °C) with zirconia-based electrolytes to account for insufficient oxygen-ion conductance (~10⁻⁸ S cm⁻¹ at 300 °C). By contrast, type III sensors with a LiPON pellet-based electrolyte²¹ (FIG. 5d) or a Li₃PO₄ thick-film electrolyte¹⁵⁴ (FIG. 5e) require a medium-to-low temperature range (<500 °C) for Li-ion conductivity (~10⁻⁸–10⁻⁶ S cm⁻¹ at ambient temperatures)^{155–157}. However, lower operating temperatures and response times (<60 s) are needed for applications of these sensors on chips and noses. The sensing speed of solid-state type III gas sensors is mainly limited by the low mobility of Li⁺ and Na⁺ ions in the solid ceramic thin-film electrolyte, in addition to slow gas-oxidation kinetics at interfaces and poor long-term chemical and structural stability under a reactive atmosphere (such as humidity and SO_x). Solid-state Li conductors with high conductivities could address these limitations.

The development of type III sensors has historically been related to progress in ceramic manufacturing and to the phase determination of fast Li-ion and Na-ion conductors primarily applied in batteries. Type III electrochemical solid-state potentiometric gas sensors using Li⁺ or Na⁺ have been explored for the detection of CO_x (FIG. 5f), SO_x (FIG. 5g) and NO_x (FIG. 5h) gas. Oxide-based Li conductors, such as Li super ionic conductor (LISICON)^{158,159}, Li₃PO₄ (REFS^{154,160–164}), garnet-type Li₆BaLa₂Ta₂O₁₂ (REF.¹⁶⁵), perovskite-type LLTO²⁵ and garnet-type LLZO²⁹, have good structural and chemical stability and sufficiently high ionic conductivities (≥10⁻⁶ S cm⁻¹ at room temperature)^{166,167} for fast sensing at low temperatures. Oxide-based Li conductors are usually processed as millimetre-sized pellets and have mainly been used for environmental CO₂ sensing thus far (FIG. 5f). Fast conductors, such as Ta-doped LLZO pellets, have also been integrated in potentiometric type III gas sensors, showing high Li-ion conductivity and good electrolyte stability, and, thus, a fast CO₂ sensing response time of <60 s at an operating temperature of ~320 °C (REF.²⁹).

In general, Li-electrolyte materials in sensors are thick (0.8–20 μm) and pellet-based or tube-based, and they require high operation temperatures and show slow response times (>60 s). For example, Na⁺-conducting NASICON electrolytes, which can be used for the detection of CO₂ (REFS^{168–176}), suffer from poor structural stability in humid environments^{176–178}, cross-sensitivity with other gaseous species¹⁷⁹ and, most importantly, the need for high operation temperatures (>400 °C)^{168,171,180}, owing to sluggish electrolyte conduction, electrode kinetics and long response times (>60 s)^{168,180,181} (FIG. 5f). SO_x sensors using stabilized zirconia^{182,183},

Na-conducting NASICON^{153,184,185}, β'' -alumina^{186–189} or other alkaline-ion-conducting materials^{190,191} (FIG. 5g) have similar problems (that is, high operating temperature, long response time and poor electrolyte stability in a SO_x environment). By contrast, state-of-the-art solid-state NO_x sensors (FIG. 5h) with perovskite-based¹⁹², zirconia-based^{193–195} or NASICON-based^{196–198} electrolytes require lower operation temperatures (~200 °C). These type III sensors are further limited by poor selectivity, stability and sensitivity in corrosive environments (Supplementary Table 1).

Li-based thin-film sensors could enable the design of cost-effective, low-power, multi-sensing arrays with a fast response, new sensing-electrode chemistries and an expanded scope of gases (for example, CO_x, SO_x and NO_x). However, this will require a reduction of the operating temperature and response time, which may be achieved by thin-film processing of Li-oxide films by wet-chemistry (Z.D.H, Y.Z., L. Miara, L. and J.L.M.R., unpublished observations) and vacuum-based³³ techniques, which allow sufficient control of the lithiation stoichiometry during manufacturing and conductivities of >10⁻⁵ S cm⁻¹ at ambient conditions. In addition, films processed at low temperature, in particular, amorphous Li phases, could reduce fabrication costs and enable integration with on-chip applications. Fabricating stable, Li-based thin films for sensors may be challenging; however, clever material selection considering electrode, electrolyte and gas chemical compatibility and adequate encapsulation solutions may resolve the stability issue, which will require multidisciplinary contributions.

Conclusions and outlook

The development of new chemistry and processing methods for solid-state Li ceramics has enabled a new generation of Li-ion batteries. The downscaling of solid-state chemistries to film form will further increase the variety of Li conductors, whose variability in terms of Li intercalation and deintercalation (for example, metal–insulator transitions through electronic-state changes) and fast solid-state ionic motion make them interesting for applications beyond batteries; for example, Li-operated memristors for neuromorphic computing and memories, and Li conductors for environmental, health and chemistry sensors. Indeed, the functionalities can be further expanded by changing the electrode electrochemistry.

The energy density, information density and operational device speed of solid-state Li applications are

greatly improved by moving away from traditional pellet and tape processing of solid Li conductors (with thicknesses in the range of millimetres to tens of micrometres) to ceramic-film manufacturing (with thicknesses in the range of 10 µm to 10 nm). Whether Li-ceramic films will ultimately be used and commercialized, similar to O²⁻-conducting functional ceramics will depend on advances in controlling Li stoichiometry and in understanding the phase evolution and interfacial phenomena with specific electrodes during Li-film preparation and device operation. In particular, interfacial reactions need to be avoided and the space-charge-layer thickness needs to be reduced to enable device miniaturization to the sub-100 nm range. With the exception of LiPON, only a few of the most promising solid-state Li conductors have been translated into films thus far. However, the film form makes these materials attractive for lithionic applications, exploiting Li motion in the solid state, which ranges from 10⁹ to 10⁵ Hz, to enable different functionalities, including ns-switching non-binary neuromorphic computing and fast-conducting solid electrolytes for high-energy-density solid-state batteries.

We envision that lithionic chip units could be made of one type of Li-conductor film. The electrochemistry could then be defined simply by varying the electrode material. For example, by reducing the size of Li ceramics from millimetres to micrometres or nanometres, a variety of new functionalities can be achieved using one type of material. From environmental and economic viewpoints, using less materials and reducing the effective ceramic mass per device volume also decreases the amount of waste and costs; for example, commercialized LiPON-based microbatteries for small-scale energy storage could also become an integral part of electrochemical sensing units or neuromorphic-computing units. Similarly, multifunctional devices, such as three-terminal computation units coupled with microbatteries (for example, Li reservoir), could combine two or more functionalities in one on-chip device unit⁵⁷.

Solid-state lithionics offer vast application opportunities based on Li ceramics in film form, whose chemistry and thermal processing can be modified to design a range of microdevices beyond batteries. Collaborations between material scientists, chemists and device engineers will lead to new material chemistries and device structures, to achieve the ambitious goal of using Li ions to power, compute and sense the world.

Published online: 26 November 2020

- Becerra, J. The digital revolution is not about technology – it's about people. *World Economic Forum* <https://www.weforum.org/agenda/2017/03/the-digital-revolution-is-not-about-technology-it-s-about-people/> (2017).
- Gerrish, H. H. *Transistor Electronics* (Goodheart-Willcox, 1969).
- Shilov, A. Samsung completes development of 5nm EUV process technology. *AnandTech* <https://www.anandtech.com/show/14231/samsung-completes-development-of-5-nm-euv-process-technology> (2019).
- Shilov, A. TSMC announces performance-enhanced 7nm & 5nm process technologies. *AnandTech* <https://www.anandtech.com/show/14687/tsmc-announces-performance-enhanced-7nm-5nm-process-technologies> (2019).
- Olofsson, A. Silicon compilers - version 2.0. *Int. Symp. Phys. Des.* <http://www.ispd.cc/slides/ispd2018.html> (2018).
- Von Neumann, J. First draft of a report on the EDVAC. *IEEE Ann. Hist. Comput.* **15**, 27–75 (1993).
- Hruska, J. Microfluidics: DARPA is betting embedded water droplets could cool next-gen chips. *ExtremeTech* <https://www.extremetech.com/extreme/224516-microfluidics-darpa-is-betting-embedded-water-droplets-could-cool-next-gen-chips> (2016).
- NanoMarkets. Opportunities for thin-film batteries. *SlideShare* <https://www.slideshare.net/NanoMarkets/thin-batteries> (2014).
- Frank, R. What's happening in air quality sensing? *Sensor Tips* <https://www.sensortips.com/featured/whats-happening-in-air-quality-sensing/> (2019).
- Maier, J. Space charge regions in solid two-phase systems and their conduction contribution. III. Defect chemistry and ionic-conductivity in thin-films. *Solid State Ion.* **23**, 59–67 (1987).
- Lacivita, V. et al. Resolving the amorphous structure of lithium phosphorus oxynitride (LiPON). *J. Am. Chem. Soc.* **140**, 11029–11038 (2018).
- Bates, J. B. et al. Rechargeable thin-film lithium microbatteries. *Solid State Technol.* **36**, 59–64 (1993).
- Johnson, R. T., Biefeld, R. M., Knotek, M. L. & Morosin, B. Ionic-conductivity in solid electrolytes based on lithium aluminosilicate glass and glass-ceramic. *J. Electrochem. Soc.* **123**, 680–687 (1976).
- Kennedy, J. H. & Yang, Y. A highly conductive Li⁺-glass system: (1-x)(0.4SiS₂-0.6Li₂S)-xLiI. *J. Electrochem. Soc.* **133**, 2437–2438 (1986).

15. Mercier, R., Malugani, J. P., Fahys, B. & Robert, G. Superionic conduction in $\text{Li}_2\text{S-P}_2\text{S}_5\text{-LiI}$ glasses. *Solid State Ion.* **5**, 663–666 (1981).
16. Pizzini, S. Ionic conductivity in lithium compounds. *J. Appl. Electrochem.* **1**, 153–161 (1971).
17. Dudney, N. J., Bates, J. B., Zuhur, R. A., Luck, C. F. & Robertson, J. D. Sputtering of lithium compounds for preparation of electrolyte thin-films. *Solid State Ion.* **53**, 655–661 (1992).
18. Bates, J. B. et al. Electrical-properties of amorphous lithium electrolyte thin-films. *Solid State Ion.* **53**, 647–654 (1992).
19. Bates, J. B. et al. Fabrication and characterization of amorphous lithium electrolyte thin films and rechargeable thin-film batteries. *J. Power Sources* **43**, 1035–110 (1993).
20. Put, B., Vereecken, P. M. & Stesmans, A. On the chemistry and electrochemistry of LIPON breakdown. *J. Mater. Chem. A* **6**, 4848–4859 (2018).
21. Lee, C., Akbar, S. A. & Park, C. O. Potentiometric CO_2 gas sensor with lithium phosphorous oxynitride electrolyte. *Sens. Actuators B Chem.* **80**, 234–242 (2001).
22. Zhao, E. Q., Ma, F. R., Guo, Y. D. & Jin, Y. C. Stable LATP/LAGP double-layer solid electrolyte prepared via a simple dry-pressing method for solid state lithium ion batteries. *RSC Adv.* **6**, 92579–92585 (2016).
23. Aono, H., Sugimoto, E., Sadaoka, Y., Imanaka, N. & Adachi, G. Ionic-conductivity of solid electrolytes based on lithium titanium phosphate. *J. Electrochem. Soc.* **137**, 1023–1027 (1990).
24. Belous, A. G., Novitskaya, G. N., Polyanetskaya, S. V. & Gornikov, Y. I. Study of complex oxides with the composition $\text{La}_{0.35}\text{Li}_{0.35}\text{TiO}_3$. *Inorg. Mater.* **23**, 412–415 (1987).
25. Yoon, J., Hunter, G., Akbar, S. & Dutta, P. K. Interface reaction and its effect on the performance of a CO_2 gas sensor based on $\text{Li}_{0.35}\text{La}_{0.55}\text{TiO}_3$ electrolyte and Li_2CO_3 sensing electrode. *Sens. Actuators B Chem.* **182**, 95–103 (2013).
26. Shi, T., Wu, J. F., Liu, Y., Yang, R. & Guo, X. Behavioral plasticity emulated with lithium lanthanum titanate-based memristive devices: habituation. *Adv. Electron. Mater.* **3**, 1700046 (2017).
27. Lee, J. Z., Wang, Z. Y., Xin, H. L. L., Wynn, T. A. & Meng, Y. S. Amorphous lithium lanthanum titanate for solid-state microbatteries. *J. Electrochem. Soc.* **164**, A6268–A6273 (2017).
28. Meesala, Y., Jena, A., Chang, H. & Liu, R. S. Recent advancements in Li-ion conductors for all-solid-state Li-ion batteries. *ACS Energy Lett.* **2**, 2734–2751 (2017).
29. Struzik, M., Garbayo, I., Pfenninger, R. & Rupp, J. L. M. A simple and fast electrochemical CO_2 sensor based on $\text{Li}_1\text{La}_2\text{Zr}_2\text{O}_{12}$ for environmental monitoring. *Adv. Mater.* **30**, 1804098 (2018).
30. Murugan, R., Thangadurai, V. & Weppner, W. Fast lithium ion conduction in garnet-type $\text{Li}_1\text{La}_2\text{Zr}_2\text{O}_{12}$. *Angew. Chem. Int. Ed.* **46**, 7778–7781 (2007).
31. Kotobuki, M., Munakata, H., Kanamura, K., Sato, Y. & Yoshida, T. Compatibility of $\text{Li}_1\text{La}_2\text{Zr}_2\text{O}_{12}$ solid electrolyte to all-solid-state battery using Li metal anode. *J. Electrochem. Soc.* **157**, A1076–A1079 (2010).
32. Wang, B., Kwak, B. S., Sales, B. C. & Bates, J. B. Ionic conductivities and structure of lithium phosphorous oxynitride glasses. *J. Non-Cryst. Solids* **183**, 297–306 (1995).
33. Pfenninger, R., Struzik, M., Garbayo, I., Stulp, E. & Rupp, J. L. M. A low ride on processing temperature for fast lithium conduction in garnet solid-state battery films. *Nat. Energy* **4**, 475–483 (2019).
34. Sastre, J. et al. Lithium garnet $\text{Li}_1\text{La}_2\text{Zr}_2\text{O}_{12}$ electrolyte for all-solid-state batteries: closing the gap between bulk and thin film Li-ion conductivities. *Adv. Mater. Interfaces* **7**, 2000425 (2020).
35. Jones, S. D., Akridge, J. R. & Shokouhi, F. K. Thin-film rechargeable Li batteries. *Solid State Ion.* **69**, 357–368 (1994).
36. Bates, J. B., Dudney, N. J., Neudecker, B., Ueda, A. & Evans, C. D. Thin-film lithium and lithium-ion batteries. *Solid State Ion.* **135**, 33–45 (2000).
37. Padhi, A. K., Nanjundaswamy, K. S. & Goodenough, J. B. Phospho-olivines as positive-electrode materials for rechargeable lithium batteries. *J. Electrochem. Soc.* **144**, 1188–1194 (1997).
38. Zhang, L. et al. The nature of lithium-ion transport in low power consumption LiFePO_4 resistive memory with graphite as electrode. *Phys. Status Solidi RRL* **12**, 1800320 (2018).
39. Nizamidin, P., Yimit, A., Abdurrahman, A. & Itoh, K. Formaldehyde gas sensor based on silver-and-yttrium-co doped-lithium iron phosphate thin film optical waveguide. *Sens. Actuators B Chem.* **176**, 460–466 (2013).
40. Lee, H., Kim, S., Kim, K. B. & Choi, J. W. Scalable fabrication of flexible thin-film batteries for smart lens applications. *Nano Energy* **53**, 225–231 (2018).
41. Mizushima, K., Jones, P. C., Wiseman, P. J. & Goodenough, J. B. Li_xCoO_2 ($0 < x \leq 1$): A new cathode material for batteries of high energy density. *Solid State Ion.* **3–4**, 171–174 (1981).
42. Wang, B. et al. Characterization of thin-film rechargeable lithium batteries with lithium cobalt oxide cathodes. *J. Electrochem. Soc.* **143**, 3203–3213 (1996).
43. Moradpour, A. et al. Resistive switching phenomena in Li_xCoO_2 thin films. *Adv. Mater.* **23**, 4141–4145 (2011).
44. Gonzalez-Rosillo, J. C. et al. Lithium-battery anode gains additional functionality for neuromorphic computing through metal–insulator phase separation. *Adv. Mater.* **32**, 1907465 (2020).
45. Thackeray, M. M., Johnson, P. J., Depiccio, L. A., Bruce, P. G. & Goodenough, J. B. Electrochemical extraction of lithium from LiMn_2O_4 . *Mater. Res. Bull.* **19**, 179–187 (1984).
46. Bates, J. B. et al. Thin-film rechargeable lithium batteries. *J. Power Sources* **54**, 58–62 (1995).
47. Morcrette, M., Barboux, P., Perriere, J. & Brousse, T. LiMn_2O_4 thin films for lithium ion sensors. *Solid State Ion.* **112**, 249–254 (1998).
48. Menetrier, M., Saadoun, I., Levasseur, S. & Delmas, C. The insulator-metal transition upon lithium deintercalation from LiCoO_2 : electronic properties and ^7Li NMR study. *J. Mater. Chem.* **9**, 1135–1140 (1999).
49. Marianetti, C. A., Kotliar, G. & Ceder, G. A first-order Mott transition in Li_xCoO_2 . *Nat. Mater.* **3**, 627–631 (2004).
50. Milewska, A. et al. The nature of the nonmetal-metal transition in Li_xCoO_2 oxide. *Solid State Ion.* **263**, 110–118 (2014).
51. Gokmen, T. & Vlasov, Y. Acceleration of deep neural network training with resistive cross-point devices: design considerations. *Front. Neurosci.* **10**, 335 (2016).
52. Wang, Z. R. et al. Resistive switching materials for information processing. *Nat. Rev. Mater.* **5**, 173–195 (2020).
53. Waser, R., Dittmann, R., Staikov, G. & Szot, K. Redox-based resistive switching memories – nanoionic mechanisms, prospects, and challenges. *Adv. Mater.* **21**, 2632–2663 (2009).
54. He, P., Yu, H. J., Li, D. & Zhou, H. S. Layered lithium transition metal oxide cathodes towards high energy lithium-ion batteries. *J. Mater. Chem.* **22**, 3680–3695 (2012).
55. Choi, J. W. & Aurbach, D. Promise and reality of post-lithium-ion batteries with high energy densities. *Nat. Rev. Mater.* **1**, 16013 (2016).
56. Antolini, E. LiCoO_2 : formation, structure, lithium and oxygen nonstoichiometry, electrochemical behaviour and transport properties. *Solid State Ion.* **170**, 159–171 (2004).
57. Fuller, E. J. et al. Li-ion synaptic transistor for low power analog computing. *Adv. Mater.* **29**, 1604310 (2017).
58. Nadkarni, N., Zhou, T. T., Fraggadakis, D., Gao, T. & Bazant, M. Z. Modeling the metal–insulator phase transition in Li_xCoO_2 for energy and information storage. *Adv. Funct. Mater.* **29**, 1902821 (2019).
59. Thackeray, M. M., David, W. I. F., Bruce, P. G. & Goodenough, J. B. Lithium insertion into manganese spinels. *Mater. Res. Bull.* **18**, 461–472 (1983).
60. Nizamidin, P., Yin, Y., Turdi, G. & Yimit, A. Characterization of the optical and gas sensitivities of a nickel-doped lithium iron phosphate thin film. *Anal. Lett.* **51**, 2039–2049 (2018).
61. Moore, S. K. Two startups use processing in flash memory for AI at the edge. *IEEE Spectrum* <https://spectrum.ieee.org/tech-talk/computing/embedded-systems/two-startups-use-processing-in-flash-memory-for-ai-at-the-edge> (2018).
62. Li, J. C., Ma, C., Chi, M. F., Liang, C. D. & Dudney, N. J. Solid electrolyte: the key for high-voltage lithium batteries. *Adv. Energy Mater.* **5**, 1401408 (2015).
63. Tarascon, J. M. & Armand, M. Issues and challenges facing rechargeable lithium batteries. *Nature* **414**, 359–367 (2001).
64. Quartarone, E. & Mustarelli, P. Electrolytes for solid-state lithium rechargeable batteries: recent advances and perspectives. *Chem. Soc. Rev.* **40**, 2525–2540 (2011).
65. Chu, S., Cui, Y. & Liu, N. The path towards sustainable energy. *Nat. Mater.* **16**, 16–22 (2017).
66. US Department of Energy. Vehicle Technologies Office annual merit review 2017 report (DOE, 2017).
67. Andre, D. et al. Future generations of cathode materials: an automotive industry perspective. *J. Mater. Chem. A* **3**, 6709–6732 (2015).
68. Ohta, S., Kobayashi, T., Seki, J. & Asaoka, T. Electrochemical performance of an all-solid-state lithium ion battery with garnet-type oxide electrolyte. *J. Power Sources* **202**, 332–335 (2012).
69. Wu, J. F., Pang, W. K., Peterson, V. K., Wei, L. & Guo, X. Garnet-type fast Li-ion conductors with high ionic conductivities for all-solid-state batteries. *ACS Appl. Mater. Interfaces* **9**, 12461–12468 (2017).
70. Ahn, B. Y. et al. Omnidirectional printing of flexible, stretchable, and spanning silver microelectrodes. *Science* **323**, 1590–1593 (2009).
71. Oudenhoven, J. F. M., Baggetto, L. & Notten, P. H. L. All-solid-state lithium-ion microbatteries: a review of various three-dimensional concepts. *Adv. Energy Mater.* **1**, 10–33 (2011).
72. Roberts, M. et al. 3D lithium ion batteries-from fundamentals to fabrication. *J. Mater. Chem.* **21**, 9876–9890 (2011).
73. Cheah, S. K. et al. Self-supported three-dimensional nanostructures for microbattery applications. *Nano Lett.* **9**, 3230–3233 (2009).
74. Perre, E. et al. Direct electrodeposition of aluminium nano-rods. *Electrochem. Commun.* **10**, 1467–1470 (2008).
75. Taberna, L., Mitra, S., Poizat, P., Simon, P. & Tarascon, J. M. High rate capabilities Fe_2O_3 -based Cu nano-architected electrodes for lithium-ion battery applications. *Nat. Mater.* **5**, 567–573 (2006).
76. Mazor, H., Golodnitsky, D., Burstein, L. & Peled, E. High power copper sulfide cathodes for thin-film microbatteries. *Electrochem. Solid-State Lett.* **12**, A232–A235 (2009).
77. Baggetto, L., Knoops, H. C. M., Niessen, R. A. H., Kessels, W. M. M. & Notten, P. H. L. 3D negative electrode stacks for integrated all-solid-state lithium-ion microbatteries. *J. Mater. Chem.* **20**, 3703–3708 (2010).
78. Pearce, A. et al. Three-dimensional solid-state lithium-ion batteries fabricated by conformal vapor-phase chemistry. *ACS Nano* **12**, 4286–4294 (2018).
79. Yao, H. B. et al. Crab shells as sustainable templates from nature for nanostructured battery electrodes. *Nano Lett.* **13**, 3385–3390 (2013).
80. Hyde, S. T. & Schröder-Turk, G. E. Geometry of interfaces: topological complexity in biology and materials. *Interface Focus* **2**, 529–538 (2012).
81. Zhu, C. et al. Highly compressible 3D periodic graphene aerogel microlattices. *Nat. Commun.* **6**, 6962 (2015).
82. Kim, C. et al. High-power aqueous zinc-ion batteries for customized electronic devices. *ACS Nano* **12**, 11838–11846 (2018).
83. Han, F. D. et al. High electronic conductivity as the origin of lithium dendrite formation within solid electrolytes. *Nat. Energy* **4**, 187–196 (2019).
84. Porz, L. et al. Mechanism of lithium metal penetration through inorganic solid electrolytes. *Adv. Energy Mater.* **7**, 1701003 (2017).
85. Westover, A. S., Dudney, N. J., Sacci, R. L. & Kalnaus, S. Deposition and confinement of Li metal along an artificial lipon–lipon interface. *ACS Energy Lett.* **4**, 651–655 (2019).
86. Dudney, N. J. Solid-state thin-film rechargeable batteries. *Mat. Sci. Eng. B* **116**, 245–249 (2005).
87. Garbayo, I. et al. Glass-type polymorphism in Li-garnet thin film solid state battery conductors. *Adv. Energy Mater.* **8**, 1702265 (2018).
88. Ahn, J. K. & Yoon, S. G. Characteristics of amorphous lithium lanthanum titanate electrolyte thin films grown by PLD for use in rechargeable lithium microbatteries. *Electrochem. Solid-State Lett.* **8**, A75–A78 (2005).
89. Li, C. L., Zhang, B. & Fu, Z. W. Physical and electrochemical characterization of amorphous lithium lanthanum titanate solid electrolyte thin-film fabricated by e-beam evaporation. *Thin Solid Films* **515**, 1886–1892 (2006).
90. Tan, D. H. S., Banerjee, A., Chen, Z. & Meng, Y. S. From nanoscale interface characterization to sustainable energy storage using all-solid-state batteries. *Nat. Nanotechnol.* **15**, 170–180 (2020).
91. Li, X. L. et al. LiNbO_3 -coated $\text{LiNi}_{0.8}\text{Co}_{0.1}\text{Mn}_{0.1}\text{O}_2$ cathode with high discharge capacity and rate performance for all-solid-state lithium battery. *J. Energy Chem.* **40**, 39–45 (2020).
92. Kim, K. J. & Rupp, J. L. M. All ceramic cathode composite design and manufacturing towards low interfacial resistance for garnet-based solid-state batteries. *Energy Environ. Sci.* <https://doi.org/10.1039/D0EE02062A> (2020).

93. Kim, K. J., Balaish, M., Wadaguchi, M., Kong, L. & Rupp, J. L. M. Solid-state Li-metal batteries: challenges and horizons of oxide and sulfide solid electrolytes and their interfaces. *Adv. Energy Mater.* <https://doi.org/10.1002/aenm.202002689> (2020).
94. Hwang, C. S. Prospective of semiconductor memory devices: from memory system to materials. *Adv. Electron. Mater.* **1**, 1400056 (2015).
95. Berggren, K. et al. Roadmap on emerging hardware and technology for machine learning. *Nanotechnology* **32**, 012002 (2020).
96. Mead, C. Neuromorphic electronic systems. *Proc. IEEE* **78**, 1629–1636 (1990).
97. Xia, Q. F. & Yang, J. J. Memristive crossbar arrays for brain-inspired computing. *Nat. Mater.* **18**, 309–323 (2019).
98. Tang, J. S. et al. Bridging biological and artificial neural networks with emerging neuromorphic devices: fundamentals, progress, and challenges. *Adv. Mater.* **31**, e1902761 (2019).
99. Chua, L. O. Memristor-the missing circuit element. *IEEE Trans. Circuits Syst.* **18**, 507–519 (1971).
100. Waser, R. & Aono, M. Nanoionic-based resistive switching memories. *Nat. Mater.* **6**, 833–840 (2007).
101. Strukov, D. B., Snider, G. S., Stewart, D. R. & Williams, R. S. The missing memristor found. *Nature* **453**, 80–83 (2008).
102. Pan, F., Gao, S., Chen, C., Song, C. & Zeng, F. Recent progress in resistive random access memories: Materials, switching mechanisms, and performance. *Mat. Sci. Eng. R Rep* **83**, 1–59 (2014).
103. Burr, G. W. et al. Overview of candidate device technologies for storage-class memory. *IBM J. Res. Dev.* **52**, 449–464 (2008).
104. Chen, Y. Y. & Petti, C. ReRAM technology evolution for storage class memory application (IEEE, 2016).
105. Burr, G. W. et al. Neuromorphic computing using non-volatile memory. *Adv. Phys X* **2**, 89–124 (2017).
106. Prezioso, M. et al. Training and operation of an integrated neuromorphic network based on metal-oxide memristors. *Nature* **521**, 61–64 (2015).
107. Borghetti, J. et al. 'Memristive' switches enable 'stateful' logic operations via material implication. *Nature* **464**, 873–876 (2010).
108. Yang, J. J. S., Strukov, D. B. & Stewart, D. R. Memristive devices for computing. *Nat. Nanotechnol.* **8**, 13–24 (2013).
109. Torrezan, A. C., Strachan, J. P., Medeiros-Ribeiro, G. & Williams, R. S. Sub-nanosecond switching of a tantalum oxide memristor. *Nanotechnology* **22**, 485203 (2011).
110. Wei, Z. et al. Demonstration of high-density ReRAM ensuring 10-year retention at 85° C based on a newly developed reliability model (IEEE, 2011).
111. Zhirnov, V. V., Meade, R., Cavin, R. K. & Sandhu, G. Scaling limits of resistive memories. *Nanotechnology* **22**, 254027 (2011).
112. Yoon, J. H. et al. Truly electroforming-free and low-energy memristors with preconditioned conductive tunneling paths. *Adv. Funct. Mater.* **27**, 1702010 (2017).
113. Messerschmitt, F., Kubicek, M., Schweiger, S. & Rupp, J. L. M. Memristor kinetics and diffusion characteristics for mixed anionic-electronic SrTiO₃-δ bits: The memristor-based Cottrell analysis connecting material to device performance. *Adv. Funct. Mater.* **24**, 7448–7460 (2014).
114. Valov, I., Waser, R., Jameson, J. R. & Kozicki, M. N. Electrochemical metallization memories—fundamentals, applications, prospects. *Nanotechnology* **22**, 254003 (2011).
115. Banno, N., Sakamoto, T., Hasegawa, T., Terabe, K. & Aono, M. Effect of ion diffusion on switching voltage of solid-electrolyte nanometer switch. *Jpn. J. Appl. Phys.* **45**, 3666–3668 (2006).
116. Kozicki, M. N. & Barnaby, H. J. Conductive bridging random access memory—materials, devices and applications. *Semicond. Sci. Technol.* **31**, 113001 (2016).
117. Yao, P. et al. Face classification using electronic synapses. *Nat. Commun.* **8**, 15199 (2017).
118. Wang, W. et al. Learning of spatiotemporal patterns in a spiking neural network with resistive switching synapses. *Sci. Adv.* **4**, eaat4752 (2018).
119. Li, Y. Y. & Chueh, W. C. Electrochemical and chemical insertion for energy transformation and switching. *Annu. Rev. Mater. Res.* **48**, 137–165 (2018).
120. Xia, H., Lu, L. & Ceder, G. Li diffusion in LiCoO₂ thin films prepared by pulsed laser deposition. *J. Power Sources* **159**, 1422–1427 (2006).
121. Stanje, B. et al. Solid electrolytes: extremely fast charge carriers in garnet-type Li₆La₂ZrTaO₁₂ single crystals. *Ann. Phys. (Berl.)* **529**, 1700140 (2017).
122. van den Broek, J., Afyon, S. & Rupp, J. L. M. Interface-engineered all-solid-state Li-ion batteries based on garnet-type fast Li⁺ conductors. *Adv. Energy Mater.* **6**, 1600736 (2016).
123. Zhu, X. J. et al. Direct observation of lithium-ion transport under an electrical field in Li_xCoO₂ nanograins. *Sci. Rep.* **3**, 1084 (2013).
124. Mai, V. H. et al. Memristive and neuromorphic behavior in a LiCoO₂ nanobattery. *Sci. Rep.* **5**, 7761 (2015).
125. Nguyen, V. S. et al. Direct evidence of lithium ion migration in resistive switching of lithium cobalt oxide nanobatteries. *Small* **14**, e1801038 (2018).
126. Greenlee, J. D. et al. *In-situ* oxygen x-ray absorption spectroscopy investigation of the resistance modulation mechanism in LiNbO₃ memristors. *Appl. Phys. Lett.* **100**, 182106 (2012).
127. Yakopcic, C. et al. Filament formation in lithium niobate memristors supports neuromorphic programming capability. *Neural Comput. Appl.* **30**, 3773–3779 (2018).
128. Greenlee, J. D. et al. Radiation effects on LiNbO₃ memristors for neuromorphic computing applications. *IEEE Trans. Nucl. Sci.* **60**, 4555–4562 (2013).
129. Wang, S. et al. Experimental study of LiNbO₃ memristors for use in neuromorphic computing. *Microelectron. Eng.* **168**, 37–40 (2017).
130. Wang, S. et al. Lithium based memristive device (IEEE, 2015).
131. Zhu, X. J. et al. In situ nanoscale electric field control of magnetism by nanoionics. *Adv. Mater.* **28**, 7658–7665 (2016).
132. Fraggadakis, D. M. M., Zhou, T. & Bazant, M. Z. Dielectric breakdown by electric-field induced phase separation. *J. Electrochem. Soc.* **167**, 11 (2020).
133. Watanabe, Y. et al. Low-energy-consumption three-valued memory device inspired by solid-state batteries. *ACS Appl. Mater. Interfaces* **11**, 45150–45154 (2019).
134. Hu, Q. et al. Lithium ion trapping mechanism of SiO₂ in LiCoO₂ based memristors. *Sci. Rep.* **9**, 5081 (2019).
135. Li, Y. Y. et al. Low-voltage, CMOS-free synaptic memory based on Li₂TiO₅ redox transistors. *ACS Appl. Mater. Interfaces* **11**, 38982–38992 (2019).
136. Speulmanns, J., Kia, A. M., Kühnel, K., Bönhardt, S. & Weinreich, W. Surface-dependent performance of ultrathin TiN films as an electrically conducting Li diffusion barrier for Li-ion-based devices. *ACS Appl. Mater. Interfaces* **12**, 39252–39260 (2020).
137. Gurney, K. R. et al. High resolution fossil fuel combustion CO₂ emission fluxes for the United States. *Environ. Sci. Technol.* **43**, 5535–5541 (2009).
138. Wang, C., Chen, J. N. & Zou, J. Decomposition of energy-related CO₂ emission in China: 1957–2000. *Energy* **30**, 73–83 (2005).
139. Joughin, I., Smith, B. E. & Medley, B. Marine ice sheet collapse potentially under way for the Thwaites Glacier Basin, West Antarctica. *Science* **344**, 735–738 (2014).
140. Feldmann, J. & Levermann, A. Collapse of the West Antarctic Ice Sheet after local destabilization of the Amundsen Basin. *Proc. Natl Acad. Sci. USA* **112**, 14191–14196 (2015).
141. Obama, B. The irreversible momentum of clean energy. *Science* **355**, 126–129 (2017).
142. Alexandre, M. & Gerboles, M. Review of small commercial sensors for indicative monitoring of ambient gas. *Chem. Eng. Trans.* **30**, 169–174 (2012).
143. Szulczynski, B. & Gebicki, J. Currently commercially available chemical sensors employed for detection of volatile organic compounds in outdoor and indoor air. *Environments* **4**, 21 (2017).
144. Dinh, T. V., Choi, I. Y., Son, Y. S. & Kim, J. C. A review on non-dispersive infrared gas sensors: Improvement of sensor detection limit and interference correction. *Sens. Actuators B Chem.* **231**, 529–538 (2016).
145. Park, C. O. & Akbar, S. A. Ceramics for chemical sensing. *J. Mater. Sci.* **38**, 4611–4637 (2003).
146. Liu, Y. X., Parisi, J., Sun, X. C. & Lei, Y. Solid-state gas sensors for high temperature applications—a review. *J. Mater. Chem. A* **2**, 9919–9943 (2014).
147. Yamazoe, N. & Miura, N. Environmental gas-sensing. *Sens. Actuators B Chem.* **20**, 95–102 (1994).
148. Maskell, W. C. Inorganic solid state chemically sensitive devices: electrochemical oxygen gas sensors. *J. Phys. E Sci. Instrum.* **20**, 1156–1168 (1987).
149. Weppner, W. Solid-state electrochemical gas sensors. *Sens. Actuators* **12**, 107–119 (1987).
150. Ramamoorthy, R., Dutta, P. K. & Akbar, S. A. Oxygen sensors: materials, methods, designs and applications. *J. Mater. Sci.* **38**, 4271–4282 (2003).
151. Chamberland, M. G. A. Solid-state detectors for the potentiometric determination of gaseous oxides. *J. Electrochem. Soc.* **124**, 1579–1583 (1977).
152. Worrell, W. L. & Liu, Q. G. A new sulphur dioxide sensor using a novel two-phase solid-sulphate electrolyte. *J. Electroanal. Chem. Interfacial Electrochem.* **168**, 355–362 (1984).
153. Akila, R. & Jacob, K. T. Use of the Nasicon/Na₂SO₄ couple in a solid state sensor for SO_x (x=2,3). *J. Appl. Electrochem.* **18**, 245–251 (1988).
154. Wang, H. R., Chen, D., Zhang, M. & Wang, J. H. Influence of the sensing and reference electrodes relative size on the sensing properties of Li₃PO₄-based potentiometric CO₂ sensors. *Surf. Coat. Technol.* **320**, 542–547 (2017).
155. Yu, X. H., Bates, J. B., Jellison, G. E. & Hart, F. X. A stable thin-film lithium electrolyte: Lithium phosphorus oxynitride. *J. Electrochem. Soc.* **144**, 524–532 (1997).
156. Su, Y. et al. LiPON thin films with high nitrogen content for application in lithium batteries and electrochromic devices prepared by RF magnetron sputtering. *Solid State Ion.* **282**, 63–69 (2015).
157. Ivanov-Shitz, A. K., Kireev, V. V., Mel'nikov, O. K. & Demianets, L. N. Growth and ionic conductivity of γ-Li₃PO₄. *Crystallogr. Rep.* **46**, 864–867 (2001).
158. Menil, F., Daddah, B. O., Tardy, P., Debeda, H. & Lucat, C. Planar LISICON-based potentiometric CO₂ sensors: influence of the working and reference electrodes relative size on the sensing properties. *Sens. Actuators B Chem.* **107**, 695–707 (2005).
159. Obata, K., Motohi, S. & Matsushima, S. NO₂ and CO₂ sensing properties of LISICON-based sensor operative at room temperature. *Sens. Mater.* **24**, 43–56 (2012).
160. Satyanarayana, L., Choi, G. P., Noh, W. S., Lee, W. Y. & Park, J. S. Characteristics and performance of binary carbonate auxiliary phase CO₂ sensor based on Li₃PO₄ solid electrolyte. *Solid State Ion.* **177**, 3485–3490 (2007).
161. Lee, H. K., Choi, N. J., Moon, S. E., Yang, W. S. & Kim, J. A solid electrolyte potentiometric CO₂ gas sensor composed of lithium phosphate as both the reference and the solid electrolyte materials. *J. Korean Phys. Soc.* **61**, 938–941 (2012).
162. Choi, N. J., Lee, H. K., Moon, S. E., Yang, W. S. & Kim, J. Stacked-type potentiometric solid-state CO₂ gas sensor. *Sens. Actuators B Chem.* **187**, 340–346 (2013).
163. Sun, G. L., Wang, H. R., Li, P., Liu, Z. & Jiang, Z. D. Response characteristics of a potentiometric CO₂ gas sensor based on Li₃PO₄ solid electrolyte using Au film as the electrodes. *J. Appl. Phys.* **115**, 124505 (2014).
164. Noh, W. S., Satyanarayana, L. & Park, J. S. Potentiometric CO₂ sensor using Li⁺ ion conducting Li₃PO₄ thin film electrolyte. *Sensors* **5**, 465–472 (2005).
165. Zhu, Y. M., Thangadurai, V. & Weppner, W. Garnet-like solid state electrolyte Li₂BaLa₂Ta₂O₁₂ based potentiometric CO₂ gas sensor. *Sens. Actuators B Chem.* **176**, 284–289 (2013).
166. Thangadurai, V., Narayanan, S. & Pinzaru, D. Garnet-type solid-state fast Li ion conductors for Li batteries: critical review. *Chem. Soc. Rev.* **43**, 4714–4727 (2014).
167. Bachman, J. C. et al. Inorganic solid-state electrolytes for lithium batteries: mechanisms and properties governing ion conduction. *Chem. Rev.* **116**, 140–162 (2016).
168. Alonso-Porta, M. & Kumar, R. V. Use of NASICON/Na₂CO₃ system for measuring CO₂. *Sens. Actuators B Chem.* **71**, 173–178 (2000).
169. Sahner, K. et al. CO₂ selective potentiometric sensor in thick-film technology. *Sensors* **8**, 4774–4785 (2008).
170. Obata, K., Kumazawa, S., Shimanoe, K., Miura, N. & Yamazoe, N. Potentiometric sensor based on NASICON and In₂O₃ for detection of CO₂ at room temperature — modification with foreign substances. *Sens. Actuators B Chem.* **76**, 639–643 (2001).
171. Dang, H. Y. & Guo, X. M. Characteristics of NASICON-based thick-film CO₂ sensor attached with integrated auxiliary electrode. *IEEE Sens. J.* **12**, 2430–2434 (2012).
172. Yao, S., Shimizu, Y., Miura, N. & Yamazoe, N. Solid electrolyte carbon dioxide sensor using sodium-ion conductor and Li₂CO₃-BaCO₃ electrode. *Jpn. J. Appl. Phys.* **31**, L197–L199 (1992).
173. Kida, T., Kishi, S., Yuasa, M., Shimanoe, K. & Yamazoe, N. Planar NASICON-based CO₂ sensor using BiCuVO₃/perovskite-type oxide as a solid-reference electrode. *J. Electrochem. Soc.* **155**, J117–J121 (2008).
174. Aono, H., Sadaoka, Y., Montanaro, L., Di Bartolomeo, E. & Traversa, E. Humidity influence on the CO₂ response of potentiometric sensors based on NASICON pellets with new compositions, Na₂Zr_{2(40/4)}Si_{2(40/4)}P_{1+x}O₁₂ (x=1.333). *J. Am. Ceram. Soc.* **85**, 585–589 (2002).

175. Kim, H. J., Choi, J. W., Do Kim, S. & Yoo, K. S. Thick-film CO₂ sensors based on NASICON synthesized by a sol-gel process. *Mater. Sci. Forum* **544**–**545**, 925–928 (2007).
176. Kida, T., Shimano, K., Miura, N. & Yamazoe, N. Stability of NASICON-based CO₂ sensor under humid conditions at low temperature. *Sens. Actuators B Chem.* **75**, 179–187 (2001).
177. Kaneyasu, K. et al. A carbon dioxide gas sensor based on solid electrolyte for air quality control. *Sens. Actuators B Chem.* **66**, 56–58 (2000).
178. Izquierdo, R. et al. Pulsed laser deposition of NASICON thin films for the fabrication of ion selective membranes. *J. Electrochem. Soc.* **144**, L323–L325 (1997).
179. Wang, L. & Kumar, R. V. Cross-sensitivity effects on a new carbon dioxide gas sensor based on solid bioelectrolyte. *Meas. Sci. Technol.* **15**, 1005–1010 (2004).
180. Hong, H. S., Kim, J. W., Jung, S. J. & Park, C. O. Suppression of NO and SO₂ cross-sensitivity in electrochemical CO₂ sensors with filter layers. *Sens. Actuators B Chem.* **113**, 71–79 (2006).
181. Salam, F., Bredikhin, S., Birke, P. & Weppner, W. Effect of the thickness of the gas-sensitive layer on the response of solid state electrochemical CO₂ sensors. *Solid State Ion.* **110**, 319–325 (1998).
182. Yan, Y. T., Shimizu, Y., Miura, N. & Yamazoe, N. High-performance solid-electrolyte SO₂ sensor using MgO-stabilized zirconia tube and Li₂SO₄·CaSO₄·SiO₂ auxiliary phase. *Sens. Actuators B Chem.* **20**, 81–87 (1994).
183. Yan, Y., Shimizu, Y., Miura, N. & Yamazoe, N. Solid-state sensor for sulfur-oxides based on stabilized zirconia and metal sulfate. *Chem. Lett.* **21**, 635–638 (1992).
184. Maruyama, T., Saito, Y., Matsumoto, Y. & Yano, Y. Potentiometric sensor for sulfur-oxides using NASICON as a solid electrolyte. *Solid State Ion.* **17**, 281–286 (1985).
185. Min, B. Y. & Choi, S. D. SO₂-sensing characteristics of Nasicon sensors with Na₂SO₄–BaSO₄ auxiliary electrolytes. *Sens. Actuators B Chem.* **93**, 209–213 (2003).
186. Rao, N., van den Bleek, C. M., Schoonman, J. & Sorensen, O. T. A novel temperature-gradient Na⁺/β⁻-alumina solid electrolyte based SO_x gas sensor without gaseous reference electrode. *Solid State Ion.* **53**, 30–38 (1992).
187. Itoh, M., Sugimoto, E. & Kozuka, Z. Solid reference electrode of SO₂ sensor using β⁻-alumina solid electrolyte. *Trans. Jpn. Inst. Met.* **25**, 504–510 (1984).
188. Yang, J. H., Yang, P. H. & Meng, G. Y. A fully solid-state SO_x (x = 2, 3) gas sensor utilizing Ag-β⁻-alumina as solid electrolyte. *Sens. Actuators B Chem.* **31**, 209–212 (1996).
189. Yang, P. H., Yang, J. H., Chen, C. S., Peng, D. K. & Meng, G. Y. Performance evaluation of SO_x (x = 2, 3) gas sensors using Ag-β⁻-alumina solid electrolyte. *Solid State Ion.* **86**–**88**, 1095–1099 (1996).
190. Wang, L. & Kumar, R. V. Potentiometric SO₂ gas sensor based on a thick film of Ca²⁺ ion conducting solid electrolyte. *J. Appl. Electrochem.* **36**, 173–178 (2006).
191. Wang, L. & Kumar, R. V. A new SO₂ gas sensor based on an Mg²⁺ conducting solid electrolyte. *J. Electroanal. Chem.* **543**, 109–114 (2003).
192. Dutta, A. & Ishihara, T. Amperometric NO_x sensor based on oxygen pumping current by using LaGaO₃-based solid electrolyte for monitoring exhaust gas. *Sens. Actuators B Chem.* **108**, 309–313 (2005).
193. Zhuiykov, S., Ono, T., Yamazoe, N. & Miura, N. High-temperature NO_x sensors using zirconia solid electrolyte and zinc-family oxide sensing electrode. *Solid State Ion.* **152**, 801–807 (2002).
194. Miura, N., Nakatou, M. & Zhuiykov, S. Impedancemetric gas sensor based on zirconia solid electrolyte and oxide sensing electrode for detecting total NO_x at high temperature. *Sens. Actuators B Chem.* **93**, 221–228 (2003).
195. Miura, N., Lu, G., Ono, M. & Yamazoe, N. Selective detection of NO by using an amperometric sensor based on stabilized zirconia and oxide electrode. *Solid State Ion.* **117**, 283–290 (1999).
196. Miura, N., Iio, M., Lu, G. Y. & Yamazoe, N. Solid-state amperometric NO₂ sensor using a sodium ion conductor. *Sens. Actuators B Chem.* **35**, 124–129 (1996).
197. Shimizu, Y. & Maeda, K. Solid electrolyte NO_x sensor using pyrochlore-type oxide electrode. *Sens. Actuators B Chem.* **52**, 84–89 (1998).
198. Yao, S., Shimizu, Y., Miura, N. & Yamazoe, N. Use of sodium-nitrite auxiliary electrode for solid electrolyte sensor to detect nitrogen-oxides. *Chem. Lett.* **21**, 587–590 (1992).
199. Orfanidou, C. M. et al. Stoichiometry and volume dependent transport in lithium ion memristive devices. *AIP Adv.* **8**, 115211 (2018).
200. Li, H. T. et al. Memristive behaviors of LiNbO₃ ferroelectric diodes. *Appl. Phys. Lett.* **97**, 012902 (2010).
201. Pan, X. Q. et al. Rectifying filamentary resistive switching in ion-exfoliated LiNbO₃ thin films. *Appl. Phys. Lett.* **108**, 032904 (2016).
202. Wu, J. F. et al. Gallium-doped Li₇Zr₂O₁₂ garnet-type electrolytes with high lithium-ion conductivity. *ACS Appl. Mater. Interfaces* **9**, 1542–1552 (2017).
203. Kwon, W. J. et al. Enhanced Li⁺ conduction in perovskite Li₃La_{2/3}□_{1/3}□_{1/3}□_{1/3}TiO₃ solid-electrolytes via microstructural engineering. *J. Mater. Chem. A* **5**, 6257–6262 (2017).
204. Furusawa, S., Tabuchi, H., Sugiyama, T., Tao, S. W. & Irvine, J. T. S. Ionic conductivity of amorphous lithium lanthanum titanate thin film. *Solid State Ion.* **176**, 553–558 (2005).
205. Bucharsky, E. C., Schell, K. G., Hintennach, A. & Hoffmann, M. J. Preparation and characterization of sol-gel derived high lithium ion conductive NZP-type ceramics Li_{1+x}Al_xTi_{2-x}(PO₄)₃. *Solid State Ion.* **274**, 77–82 (2015).
206. Chen, H. P., Tao, H. Z., Zhao, X. J. & Wu, Q. D. Fabrication and ionic conductivity of amorphous Li–Al–Ti–P–O thin film. *J. Non-Cryst. Solids* **357**, 3267–3271 (2011).
207. Zhu, Y. Z., He, X. F. & Mo, Y. F. Origin of outstanding stability in the lithium solid electrolyte materials: insights from thermodynamic analyses based on first-principles calculations. *ACS Appl. Mater. Interfaces* **7**, 23685–23693 (2015).
208. Julien, C. M., Mauger, A., Zaghib, Z. & Groult, H. Comparative issues of cathode materials for Li-ion batteries. *Inorganics* **2**, 132–154 (2014).
209. Min, H. S. et al. Fabrication and properties of a carbon/polypropylene three-dimensional microbattery. *J. Power Sources* **178**, 795–800 (2008).
210. Nishizawa, M., Mukai, K., Kuwabata, S., Martin, C. R. & Yoneyama, H. Template synthesis of polypyrrole-coated spinel LiMn₂O₄ nanotubes and their properties as cathode active materials for lithium batteries. *J. Electrochem. Soc.* **144**, 1923–1927 (1997).
211. Kotobuki, M. et al. Electrochemical property of honeycomb type all-solid-state Li battery at high temperature. *Electrochemistry* **79**, 464–466 (2011).
212. Shajumon, M. M. et al. Nanoarchitected 3D cathodes for Li-ion microbatteries. *Adv. Mater.* **22**, 4978–4981 (2010).
213. Mazar, H., Golodnitsky, D., Burstein, L., Gladkikh, A. & Peled, E. Electrophoretic deposition of lithium iron phosphate cathode for thin-film 3D-microbatteries. *J. Power Sources* **198**, 264–272 (2012).
214. Kim, H., Proell, J., Kohler, R., Pflöging, W. & Pique, A. Laser-printed and processed LiCoO₂ cathode films for Li-ion microbatteries. *J. Laser Micro Nanoeng.* **7**, 320–325 (2012).
215. Gowda, S. R., Reddy, A. L. M., Zhan, X. B., Jafry, H. R. & Ajayan, P. M. 3D nanoporous nanowire current collectors for thin film microbatteries. *Nano Lett.* **12**, 1198–1202 (2012).
216. Lai, W. et al. Ultrahigh-energy-density microbatteries enabled by new electrode architecture and micropackaging design. *Adv. Mater.* **22**, E139–E144 (2010).
217. Yoshida, K., Munakata, H. & Kanamura, K. Fabrication of micro lithium-ion battery with 3D anode and 3D cathode by using polymer wall. *J. Power Sources* **208**, 404–408 (2012).
218. Pikul, J. H., Zhang, H. G., Cho, J., Braun, P. V. & King, W. P. High-power lithium ion microbatteries from interdigitated three-dimensional bicontinuous nanoporous electrodes. *Nat. Commun.* **4**, 1732 (2013).
219. Gaikwad, A. M., Whiting, G. L., Steingart, D. A. & Arias, A. C. Highly flexible, printed alkaline batteries based on mesh-embedded electrodes. *Adv. Mater.* **23**, 3251–3255 (2011).
220. Nathan, M. et al. Three-dimensional thin-film Li-ion microbatteries for autonomous MEMS. *J. Microelectromech. Syst.* **14**, 879–885 (2005).
221. Sun, K. et al. 3D printing of interdigitated Li-ion microbattery architectures. *Adv. Mater.* **25**, 4539–4543 (2013).
222. Wang, Z. R. et al. Fully memristive neural networks for pattern classification with unsupervised learning. *Nat. Electron.* **1**, 137–145 (2018).
223. Ma, C. et al. Sub-ppb SO₂ gas sensor based on NASICON and LaSm_{1-x}FeO₃ sensing electrode. *Sens. Actuators B Chem.* **256**, 648–655 (2018).
224. Izu, N., Hagen, G., Schonauer, D., Roder-Roith, U. & Moos, R. Planar potentiometric SO₂ gas sensor for high temperatures using NASICON electrolyte combined with V₂O₅/WO₃/TiO₂ + Au or Pt electrode. *J. Ceram. Soc. Jpn.* **119**, 687–691 (2011).
225. Wang, L. & Kumar, R. V. A SO₂ gas sensor based upon composite Nasicon/Sr-β⁻-Al₂O₃ bioelectrolyte. *Mater. Res. Bull.* **40**, 1802–1815 (2005).
226. Mari, C. M., Beghi, M., Pizzini, S. & Faltemier, J. Electrochemical solid-state sensor for SO₂ determination in air. *Sens. Actuators B Chem.* **2**, 51–55 (1990).
227. Wang, H., Liu, Z., Chen, D. & Jiang, Z. A new potentiometric SO₂ sensor based on Li₃PO₄ electrolyte film and its response characteristics. *Rev. Sci. Instrum.* **86**, 075007 (2015).
228. Chen, K. D., Zhang, M., Wang, H. R. & Gu, H. Q. A potentiometric SO₂ gas sensor based on the Li₃PO₄-Li₂SiO₄ solid electrolyte thin film. *Rev. Sci. Instrum.* **90**, 065001 (2019).
229. White, B., Chatterjee, S., Macam, E. & Wachsmann, E. Effect of electrode microstructure on the sensitivity and response time of potentiometric NO_x sensors. *J. Am. Ceram. Soc.* **91**, 2024–2031 (2008).
230. Zhuiykov, S., Nakano, T., Kunimoto, A., Yamazoe, N. & Miura, N. Potentiometric NO_x sensor based on stabilized zirconia and NiCr₂O₄ sensing electrode operating at high temperatures. *Electrochem. Commun.* **3**, 97–101 (2001).
231. Mondal, S. P. et al. Development of high sensitivity potentiometric NO_x sensor and its application to breath analysis. *Sens. Actuators B Chem.* **158**, 292–298 (2011).
232. Miura, N., Lu, G. Y. & Yamazoe, N. High-temperature potentiometric/amperometric NO_x sensors combining stabilized zirconia with mixed-metal oxide electrode. *Sens. Actuators B Chem.* **52**, 169–178 (1998).
233. Romanytsia, I., Viricelle, J. P., Vernoux, P. & Pijolat, C. Application of advanced morphology Au–X (X = YSZ, ZrO₂) composites as sensing electrode for solid state mixed-potential exhaust NO_x sensor. *Sens. Actuators B Chem.* **207**, 391–397 (2015).
234. Yoo, J., Chatterjee, S. & Wachsmann, E. D. Sensing properties and selectivities of a WO₃/YSZ/Pt potentiometric NO_x sensor. *Sens. Actuators B Chem.* **122**, 644–652 (2007).
235. Obata, K. & Matsushima, S. NASICON-based NO₂ device attached with metal oxide and nitrite compound for the low temperature operation. *Sens. Actuators B Chem.* **130**, 269–276 (2008).

Acknowledgements

Y.Z., J.C.G.-R., Z.D.H. and K.J.K. were supported by Samsung Electronics, NGK Inc., Swiss National Science Foundation (grant no. BSSG10_155986) and National Science Foundation MRSEC Program (grant no. DMR-1419807). M.B. acknowledges financial support from the US-Israel Fulbright Program, the Zuckerman Israeli Postdoctoral Scholars Program and the MIT-Technion Postdoctoral Fellowship. J.L.M.R. thanks the Thomas Lord Foundation for financial support. The authors thank A. Westover for the fruitful discussions and final proofreading.

Author contributions

All authors contributed to the research and discussion of data, figure preparation and proofreading of the manuscript. Y.Z. contributed to the writing and editing of all sections of the manuscript. J.C.G.-R. wrote the Li-controlled electronic configurations and Neuromorphic computing with Li sections. M.B. contributed to the writing of the Solid-state electrochemical sensors and the editing of the Solid-state Li-conducting films sections. Z.D.H. contributed to the writing of the Solid-state thin-film batteries and the editing of the Solid-state electrochemical sensors sections. K.J.K. contributed to the writing of the Solid-state Li-conducting films section. J.L.M.R. initiated the concept for the ‘lithionics’, discussed, edited and revised the manuscript in all parts.

Competing interests

The authors declare no competing interests.

Publisher's note

Springer Nature remains neutral with regard to jurisdictional claims in published maps and institutional affiliations.

Supplementary information

Supplementary information is available for this paper at <https://doi.org/10.1038/s41578-020-00261-0>.

RELATED LINKS

Memristors to Machine Intelligence: <https://knowm.org/>